

Article

Early-Cycle Lifetime Prediction of LFP Batteries Using a Semi-Empirical Model and Chaotic Musical-Chairs Optimization

Zeyad A. Almutairi ^{1,2}, Hady A. Bheyan ¹, H. Al-Ansary ² and Ali M. Eltamaly ^{1,*}

¹ Sustainable Energy Technology Center, King Saud University, Riyadh 11421, Saudi Arabia

² Mechanical Engineering Department, King Saud University, Riyadh 11421, Saudi Arabia

* Correspondence: eltamaly@ksu.edu.sa

Abstract

Efficiently predicting the lifespan of lithium iron phosphate (LFP) batteries early in their operational life is critical to accelerating the development of energy storage systems while reducing testing time, cost, and resource consumption. Traditional degradation models rely on full-cycle testing to estimate long-term performance, which is both time- and resource-intensive. This study proposes a novel semi-empirical degradation model that leverages a small fraction of early-cycle data with just 5% to accurately forecast full-lifetime performance with high accuracy, with less than 1.5% mean absolute percentage error. The model integrates fundamental degradation physics with data-driven calibration, using an improved musical chairs algorithm modified with chaotic map dynamics to optimize model parameters efficiently. Trained and validated on a diverse dataset of 27 LFP cells cycled under varying depths of discharge, current rates, and temperatures, the proposed method demonstrates superior convergence speed, robustness across LFP operating conditions, and predictive accuracy compared to traditional approaches. These results provide a scalable framework for rapid battery evaluation and deployment, supporting advances in electric mobility and grid-scale storage.



Academic Editor: Kwok Tong Chau

Received: 14 November 2025

Revised: 29 November 2025

Accepted: 10 December 2025

Published: 12 December 2025

Citation: Almutairi, Z.A.; Bheyan, H.A.; Al-Ansary, H.; Eltamaly, A.M. Early-Cycle Lifetime Prediction of LFP Batteries Using a Semi-Empirical Model and Chaotic Musical-Chairs Optimization. *Energies* **2025**, *18*, 6528. <https://doi.org/10.3390/en18246528>

Copyright: © 2025 by the authors. Licensee MDPI, Basel, Switzerland. This article is an open access article distributed under the terms and conditions of the Creative Commons Attribution (CC BY) license (<https://creativecommons.org/licenses/by/4.0/>).

1. Introduction

The global transition from conventional fossil-fuel-based power generation to renewable energy sources (RESs) has become a strategic priority for many nations. RESs, such as solar and wind energy, offer sustainability benefits but are inherently intermittent due to their dependence on environmental conditions like solar irradiance and wind speed. This variability poses significant challenges to power systems, affecting their stability, reliability, and resilience, and often leading to frequency fluctuations [1,2].

To mitigate these issues, various grid-balancing strategies have been explored. Among the most effective is the integration of battery energy storage systems (BESS), which provide a buffer between energy generation and consumption. Lithium-ion batteries (LIBs), in particular, have emerged as the leading BESS technology, owing to their high energy and power density, long cycle life, and superior efficiency [3,4].

LIBs now serve a wide range of applications, from portable electronics and electric vehicles to utility-scale energy storage. However, like all electrochemical systems, they degrade over time. This degradation manifests as a reduction in capacity and an increase in internal resistance, resulting from a complex interplay of electrochemical and mechanical

processes influenced by usage patterns, temperature, material properties, and environmental conditions [5,6].

For LIBs to be effectively deployed in energy systems, accurate degradation modeling is essential. Reliable models enable informed decision-making about system design, operational planning, and cost-benefit analysis, including warranty estimations and lifecycle cost assessments. Crucially, the degradation behavior of LIBs varies with their chemistry, manufacturing processes, and operating conditions. As a result, degradation models must be tailored to specific battery types and use cases.

Several recent studies have explored early-life prediction models that attempt to forecast the full degradation trajectory using limited cycling data [7–12]. While promising, many of these models overlook key degradation stressors such as depth of discharge (DoD), current rate (C_{rate}), and temperature, which are addressed in the present study.

Conventional approaches typically require cells to be cycled to their end-of-life (EoL) to extract degradation parameters. This process is time-consuming, resource-intensive, and impractical for high-throughput applications [13–18]. Motapon et al. [19] proposed a model that utilizes only the first 5% of cycling data to estimate battery lifetime, significantly reducing the experimental burden. However, this method does not evaluate whether this early fraction is optimal for degradation modeling, nor does it compare predictive accuracy across different early-life data percentages.

Despite advances in semi-empirical and machine-learning models, many still rely on full-cycle or extensive partial-cycle datasets [13–18]. Reducing the dependency on prolonged testing remains a pressing challenge. A key question that remains largely unanswered is as follows: What is the minimal percentage of early-life degradation data required to reliably predict the entire lifespan of a battery?

This study proposes a novel, data-efficient degradation modeling approach that predicts a full battery lifetime from a limited portion of early-cycle data. By systematically analyzing performance across various stress conditions, we aim to identify the minimum early-life data threshold necessary to maintain prediction errors within acceptable limits. This proposed approach enables accelerated battery testing and informed deployment strategies without compromising forecast accuracy.

1.1. A Classification of LIBs Degradation Models

Researchers have developed various LIB degradation models, broadly classified by their approach to capturing underlying mechanisms. Empirical or data-driven models [20,21] fit experimental data with mathematical functions (e.g., linear [22], polynomial [23], exponential [24,25], logarithmic [26], and Arrhenius-based models [25]), offering simplicity but limited extrapolation accuracy due to a lack of mechanistic understanding. Semi-empirical models bridge this gap by incorporating some physical understanding.

Physical or electrochemical (mechanism-based) models describe fundamental degradation processes like Solid Electrolyte Interphase (SEI) layer growth, lithium plating, and active material loss, providing higher accuracy and generalizability but requiring significant computational resources and detailed knowledge [27,28]. Hybrid models combine empirical and physical approaches to balance efficiency and accuracy, often using physical principles to guide empirical functions [29].

More recently, machine learning models (e.g., neural networks, support vector machines) have emerged, leveraging algorithms to learn complex degradation patterns from data. While potentially highly accurate, their performance depends on data quality and interpretability can be limited [7,30]. Transfer learning aims to improve the generalizability of these models [31].

1.2. Literature Review

Accurate prediction of LIB cycle life using early degradation data is of critical importance across battery design, validation, and deployment phases. This predictive capability not only facilitates early screening of battery chemistries and cell designs but also enables cost-effective planning for maintenance, warranty, and recycling logistics. In response to this need, a diverse body of literature has emerged, exploring data-driven, semi-empirical, and hybrid approaches to early-life prediction.

1.2.1. Early-Cycle Data-Driven Prediction

Multiple studies have demonstrated that meaningful battery life prediction can be achieved with minimal early-cycle data. For example, Severson et al. [7] used features extracted from the first 100 cycles of commercial LFP cells and achieved a test error of around 9%. Remarkably, using only the first 5 cycles enabled the classification of battery life into “short” or “long” categories with 95% accuracy. Similarly, Li et al. [8] showed that machine learning models could predict NMC/graphite cell lifespans with less than 15% MAPE using only 15% of the total cycle data, with Bayesian techniques further generalizing to unseen cells.

Sugiarto et al. [9] highlighted the predictive value of early temperature features, achieving similar performance with just 10 initial cycles, while Celik et al. [10] achieved 99.81% accuracy in cycle life prediction of LFP cells using tree-based models and carefully engineered early-cycle features. These results emphasize a common finding: degradation trends become statistically discernible very early in a battery’s life, often within 5–15% of total cycles.

1.2.2. Semi-Empirical and Physics-Guided Models

While purely data-driven approaches offer high predictive power, they often lack interpretability and may struggle under out-of-distribution conditions. To address this, several studies have proposed semi-empirical models that incorporate electrochemical degradation principles. Nájera et al. [11] developed an online model accounting for calendar and cycling fade, achieving less than 3% error after 2000 cycles. Kim et al. [12] integrated wavelet transforms with a semi-empirical model, significantly enhancing early-life rest of useful life (RUL) prediction accuracy.

Yarimca and Cetkin [32] reviewed semi-empirical aging models for various chemistries and operating conditions, concluding that their physical grounding enables broader applicability with less data. In many cases, formal diagnostic cycles or physics-informed features can reduce reliance on large datasets while retaining extrapolation capabilities.

1.2.3. Hybrid and Machine Learning Approaches

Hybrid models that blend physical insights with machine learning have shown increasing promise. Zhang et al. [33] and Kim et al. [12] used hybrid random forest-general regression neural networks (RF-GRNN) and wavelet-enhanced frameworks, respectively, to mitigate non-linearity and noise while preserving data efficiency. More recent architectures such as ARCANA [34] and BatLiNet [35] use attention mechanisms and inter-cell learning to generalize across chemistries, charging strategies, and environmental conditions.

Notably, Zhang et al. [36] employed quantile regression forests (QRF) to generate uncertainty-aware forecasts, achieving over 95% prediction interval coverage on held-out cells. Similarly, Haris et al. [37] and Choi et al. [38] developed methods based on first-cycle and early-hundred-cycle features to train neural networks and regression models for accurate early-lifetime prediction.

Recent work by Kohtz et al. [39] and Zhang et al. [40] emphasizes the growing trend toward probabilistic and physics-informed models that maintain strong performance even when early-cycle data is limited or noisy. These models combine domain knowledge with neural architectures to produce both accurate and uncertainty-aware forecasts. In parallel, Chou et al. [41] applied attention-based transfer learning to LFP datasets, demonstrating the feasibility of lifetime prediction across different usage conditions using only a few initial cycles.

1.2.4. Gaps and Research Opportunities

Despite progress, key gaps remain where most prior works focus on average-case performance or specific chemistries under idealized cycling. Few studies systematically assess how much early-cycle data is sufficient under varying operational stressors (e.g., DoD , C_{rate} , temperature), nor do they provide robust performance trade-offs between prediction accuracy and data quantity.

Moreover, several studies rely on datasets with relatively homogeneous cell populations or cycling protocols, limiting model generalizability. Only a handful, such as Severson et al. [7] and Celik et al. [10], address variability in stress profiles and measurement noise. These limitations underscore the need for generalized models validated across diverse stress conditions using minimal early-life data which is the goal this study addresses through a unified semi-empirical framework calibrated via modified global optimization generalized across LFP stress conditions.

1.2.5. Relevance to LFP Chemistry

The distinct electrochemical behavior of LFP cells, such as flat voltage profiles and strong thermal stability, demands specialized modeling. Prior LFP-focused studies [7,10,11] confirm that early-life features from LFP cells can be highly predictive when appropriately modeled. Our work builds on these findings, using an LFP-exclusive dataset across diverse operating conditions to develop a data-efficient model that balances accuracy, generalizability, and interpretability. Parameters derived here are LFP-specific; cross-chemistry applicability is for future work.

LFP cells possess electrochemical characteristics that make their aging behavior distinct from chemistries such as NMC, limiting the applicability of traditional empirical or ML-based models. LFP's prolonged two-phase voltage plateau reduces curvature in the voltage curve, weakening the sensitivity of voltage-based features such as dV/dt , IC peaks, and early-cycle voltage signatures. Models relying on these features often lose resolution when applied to LFP. Because LFP exhibits a smaller entropy change, temperature-dependent degradation terms show weaker observable variation. Standard Arrhenius-based or thermally weighted models calibrated on NMC may therefore misrepresent LFP aging rates.

Compared with NMC, LFP shows less SEI growth and more cathode structural evolution. This shifts the relative contributions of capacity-loss and resistance-growth mechanisms, meaning NMC-tuned formulations cannot be transferred directly.

1.3. Study Motivation

The motivation for this study arises from the growing demand for efficient, accurate, and data-efficient methods for predicting LIB degradation, particularly LFP batteries, which are widely adopted in electric vehicles and grid-scale energy storage. Traditional approaches to degradation modeling require extensive and prolonged cycling to the EoL of the battery, which is both time-consuming and costly.

Emerging research has shown promising results in early-life prediction using limited cycling data; however, these methods often either lack generalizability across varying stress conditions or require large training datasets. Additionally, many prior studies do not

provide a clear understanding of how little early-cycle data is sufficient to ensure accurate lifetime forecasting. This study is driven by the need to fill this gap, enabling accelerated testing and informed decision-making for battery deployment with significantly reduced experimental effort and cost.

1.4. Innovation and Contribution

This research introduces several key innovations and contributions to the field of LIB degradation modeling:

- A novel semi-empirical degradation model is proposed that integrates fundamental degradation physics with a data-driven calibration using minimal early-cycle data.
- The study advances the musical chairs algorithm (MCA) by incorporating chaotic maps to improve exploration capabilities and convergence behavior during parameter optimization.
- Unlike previous studies, this work systematically examines the minimum percentage of early-life data needed to achieve acceptable prediction accuracy. The results show that high prediction accuracy ($MAPE < 1.5\%$) can be achieved using only 5% of the battery's early-cycle data.
- The model is validated across a diverse set of 27 LFP cell experiments with varying DoD , C_{rate} , and temperature, confirming its robustness under different stress conditions.

These contributions not only enhance the understanding of battery aging mechanisms but also provide a practical tool for industry stakeholders to reduce testing costs and expedite battery design and deployment.

1.5. Study Outlines

This paper is structured to first review existing empirical, semi-empirical, and machine learning degradation models in Section 2, followed by the introduction of a novel degradation model incorporating stress factors and a revised equivalent full cycles (EFC) framework in Section 3. Section 4 then details the modified musical chairs optimization algorithm, enhanced with chaotic maps, used in the study. The experimental setup and methodology, including battery specifications and cycling conditions, are described in Section 5, leading to Section 6 which presents and discusses the results of validating the developed degradation model using both complete and partial early-cycle data. Finally, Section 7 summarizes the study's key findings and proposes avenues for future research.

2. Degradation Models Overview

2.1. Empirical LIBs Degradation Models

Empirical models predict battery degradation by fitting experimental data to mathematical functions without considering the underlying physical or electrochemical processes. While simple and computationally efficient, these models often fail under extreme operating conditions due to their lack of physical fidelity. These models are straightforward but are limited in extrapolation and often lack stressor integration. They may yield useful fits for in-range interpolation but generally perform poorly under real-world variability. A comprehensive comparison between different empirical models has been introduced in [42]. Common empirical formulations include the following:

Linear Model: This model calculates the degradation of the batteries linearly with the number of cycles, as shown in Equation (1). This model assumes a constant rate of capacity fade over time or cycles [22,43]. This model overlooked all stress parameters such as DoD , C_{rate} , and temperature and considered only the operating time t . This model is not accurate and it cannot be used with modern BESS degradation models.

$$Q(t) = Q_0 - k \cdot t \quad (1)$$

where $Q(t)$ is the capacity at time t , Q_0 is the initial or beginning of life (BoL) capacity, k is a degradation rate parameter, and t is the time or number of cycles.

Polynomial Model: This model allows for more complex, non-linear degradation patterns. A quadratic model ($n = 2$) is frequently used, as shown in Equation (2) [23].

$$Q(t) = Q_0 - k_1 \cdot t - k_2 \cdot t^2 - \dots - k_n \cdot t^n \quad (2)$$

where k_1, k_2, k_n are coefficients determined by fitting to experimental data, n is the degree of the polynomial.

Exponential Model: This model represents a decreasing exponential decay of capacity over time [24]. In the form of an exponential form, Almutairi et al. introduced an Arrhenius-based model to estimate the degradation of two different LIBs, as shown in Equations (3) and (4) [25].

$$Q(t) = Q_0 - e^{(-b \cdot t)} \quad (3)$$

where b is a degradation rate constant

$$Q(t) = Q_0 - k e^{(-\frac{E_a}{RT} t)} \quad (4)$$

where k is the pre-exponential factor, E_a is the activation energy, R is the ideal gas constant, and T is the absolute temperature.

Logarithmic Model: This model describes capacity fade that increases with the logarithm of time or cycle number [26], as shown in Equation (5).

Formula:

$$Q(t) = Q_0 - k \cdot \ln(t) \quad (5)$$

where k is a degradation rate parameter.

2.2. Semi-Empirical Degradation Models

Semi-empirical models combine data-driven fitting with physical insight, offering a balance between accuracy and interpretability. They typically incorporate known stress factors such as temperature, C_{rate} , and DoD while using fitted parameters to capture system behavior.

Gailani et al. [44] applied semi-empirical models in grid-scale scenarios, while Zarei-Jelyani et al. [45] used a power-law framework optimized via the Marquardt–Levenberg algorithm. These models improve prediction reliability over purely empirical models while maintaining manageable computational complexity.

Model Based on Ah-Throughput: Accounts for degradation due to cycling, incorporating DoD , C_{rate} , and temperature as shown in Equation (6) [46].

$$Q(t) = Q_0 - k(Ah_t)^m e^{(-\frac{E_a}{RT})} \quad (6)$$

where Ah_t is the total Ampere-hour during the cycling, m is the exponent parameter, and k is a fitting parameter,

Stress-Factor Integrated Model: The study's main innovation is a unified aging model for Li(NiMnCo)O₂ 18,650 batteries integrating multiple degradation mechanisms. Its key contribution is a more holistic and potentially accurate prediction of battery lifespan by considering the combined effects of calendar and cycle aging under varying conditions, offering a more realistic tool for battery management than single-mechanism models, as shown in Equation (7) [47].

$$Q(t) = Q_0 - k \cdot D^\alpha e^{(-\frac{E_a}{RT})} \cdot N^\beta \quad (7)$$

where D is the DoD , N is the number of cycles, and α and β are the empirical model's parameters.

Calendar Plus Cycle Aging Model: Another study introduced a formula to determine the degradation in capacity based on the degradation due to the calendar and cycling aging as shown in Equation (8) [25,48,49].

$$Q(t) = Q_0 - k_1 e^{(-\frac{E_a}{Rt})} t^{\gamma_1} - k_2 C_{rate}^{\gamma} D^{\delta} N^{\zeta_2} \quad (8)$$

2.3. Equivalent Full Cycles

Equivalent Full Cycles (*EFCs*) are a crucial concept for empirically modeling LIB degradation, aiming to standardize diverse cycling conditions (varying DoD , C_{rate} , and temperature) to a base cycle of 0–100% *SoC*. Existing literature introduces *EFCs* as a means to quantify usage-related aging by converting operational patterns into equivalent full charge–discharge cycles [50], simplifying lifespan prediction despite real-world complexities. However, the basic *EFC* model offers a limited understanding of underlying electrochemical mechanisms, prompting researchers to expand it by incorporating factors like temperature, *SoC*, and energy throughput. One definition of *EFC* [50,51] is the ratio of actual throughput to nominal throughput at base conditions, as shown in Equation (9), but it overlooks key stress factors. Dufo-López et al. [52] proposed *EFC* as the summation of DoD over cycles, as shown in Equation (10), while also neglecting C_{rate} and temperature. For complex loads, the rainflow counting algorithm decomposes usage into cycles with varying DoD [53], again primarily focusing on DoD . While traditionally using average stress, a modified rainflow approach for LIBs Equation (11) utilizes maximum and minimum DoD within a cycle group, with *SoC* often estimated by methods like the Unscented Kalman Filter (UKF) to evaluate battery load based on average DoD (D_m) [53]. Despite these advancements, many *EFC* formulations still lack a comprehensive consideration of all significant stress factors affecting LIB degradation.

$$EFC = \sum_i^n \frac{\Delta Q}{Q_0} \quad (9)$$

where n is the number of data points applied to this equation.

$$EFC = \sum_i^n DoD_i \quad (10)$$

$$D_m = \frac{1 - D_{min} + D_{max}}{2} \quad (11)$$

where D_{max} and D_{min} are the maximum and minimum *DoD* within a cycle group.

2.4. Proposed Equivalent Full Cycles (*EFCs*)

To address non-uniform cycling observed in practical operations, this study proposes a new *EFC* mapping that captures random DoD behavior by estimating an equivalent uniform cycle. This is defined by averaging DoD over cycling windows and incorporating temperature and C_{rate} modifiers. Figure 1 illustrates the inconsistency of real-world *DoD* patterns, while Figure 2 demonstrates how these are mapped into equivalent uniform cycles using the proposed method.

This novel approach forms the foundation for the degradation model introduced in Section 3, aligning observed capacity loss with operationally normalized cycle equivalents while enabling accurate degradation forecasting with limited early-cycle data.

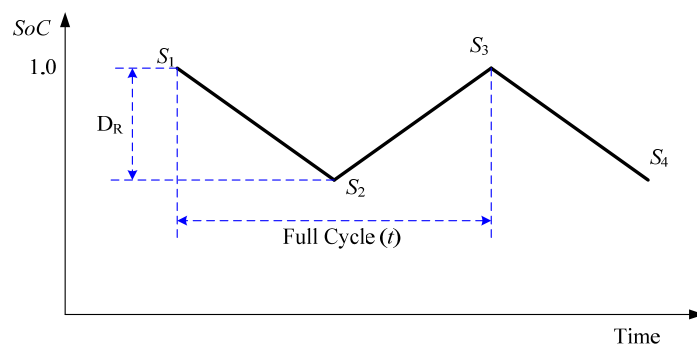


Figure 1. Battery cycling representation based on the Wohler curve.

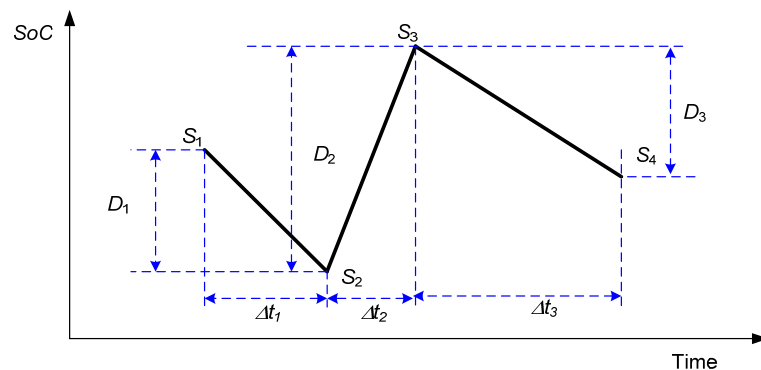


Figure 2. Illustration of random battery cycling.

2.5. Comparative Analysis of Early Prediction Modeling Approaches

Early-cycle lifetime prediction can be approached using four major classes of models: empirical, physical (mechanistic), semi-empirical, and machine learning (ML). Each class offers distinct strengths but also carries limitations in terms of data requirements, computational feasibility, interpretability, and robustness across operating conditions. Table 1 summarizes the relative strengths of these approaches, followed by a comparative discussion.

Table 1. Comparison of common early-life battery prediction approaches.

Model Type	Data Efficiency	Generalization Capability	Computational Cost	Interpretability	Sensitivity to Stressors (DoD, C-Rate, T)	Typical Limitations
Empirical Models	High (few cycles required)	Low (poor extrapolation)	Very low	Low–Moderate	High	Fail under unseen conditions; limited physical meaning
Physical (Mechanistic) Models	Low (require detailed parameterization)	High (chemistry-aware)	Very high (multi-physics)	High	Low–Moderate	Computationally intensive; require extensive cell characterization
Machine Learning Models	Very high (requires large datasets)	Moderate when in-distribution	Moderate–High	Low	High	Limited extrapolation; opaque reasoning; needs diverse training data
Semi-Empirical Models (this study)	High (5–15% early data)	Moderate–High	Low–Moderate	High	Low–Moderate	Requires parameter optimization and stress factor formulation

Empirical models offer simplicity and fast computation but generally fail to predict long-term behavior under varying temperatures, Cycles, and depths of discharge. Their lack of physical grounding limits their extrapolation capability, making them unsuitable for applications requiring stress-dependent lifetime forecasting.

Physical or mechanistic models provide the highest interpretability and generalizability because they explicitly represent degradation pathways such as SEI evolution, lithium plating, or cathode structural changes. However, they require extensive electrochemical characterization, large parameter sets, and computationally demanding simulations that make them impractical for rapid early-life screening.

Machine learning models have shown excellent performance when trained on large and diverse datasets. However, their prediction accuracy tends to degrade when tested outside the training distribution. Moreover, model interpretability remains limited, and their performance is highly sensitive to measurement noise and data preprocessing choices.

The semi-empirical approach adopted in this study offers a balanced middle ground. By embedding physically inspired stress factors (DoD , C_{rate} , and temperature) into a compact parametric structure, the model achieves the following:

- Low data requirements (high accuracy with only 5% early-cycle data);
- Reduced computational complexity compared to mechanistic or ML models;
- High interpretability, since each parameter corresponds to a known degradation stressor;
- Robustness across diverse stress conditions due to physics-guided formulation;
- Improved generalization relative to empirical models.

This comparative analysis highlights that the proposed semi-empirical degradation model is particularly suitable for rapid early-life prediction and large-scale battery screening, offering a strong combination of accuracy, efficiency, and physical relevance.

3. Developed Degradation Model

Recent advancements in LIB degradation modeling have achieved significant improvements by integrating multiple stress factors. A prominent framework, initially proposed by Serrao et al. [14] and subsequently refined by Wan et al. [18], is considered a benchmark, incorporating the combined effects of DoD , C_{rate} , and temperature [14,18,54].

Serrao et al. [14] introduced a degradation model (Equation (12)) to estimate the maximum cycle life of the battery under various stress conditions (DoD , C_{rate} , and temperature).

$$N_c(D, P_B^i, T) = \frac{N_r(D_r)}{\theta(D, I_B^i, T)} = N_r(D_r) \cdot \left(\frac{D}{D_r}\right)^{-1/\alpha} \left(\frac{I_B^i}{I_B^R}\right)^{-1/\beta} \times e^{[-\psi(\frac{1}{T^R} - \frac{1}{T})]} \quad (12)$$

Here, α , β , and ψ are parameters characterizing the impact of DoD , C_{rate} , and temperature on degradation, respectively. D_r and N_r represent the reference DoD and the corresponding cycle life at the battery's EoL under rated C_{rate} and ambient temperature (25 °C). These reference values can be obtained from cycling tests at EoL or from Wohler curves (relating cycle number to DoD). In this study, D_r and N_r are determined from cycling tests at $DoD = 1$, $C_{rate} = 1$, and temperature = 25 °C (840 cycles from cycling experimental results).

Where α , β , and ψ are the degradation model parameters of DoD , C_{rate} , and temperature, respectively, D_r and N_r are the reference DoD and number of cycles to the EoL of the battery which can be obtained from the cycling tests at the EoL of the battery at rated C_{rate} and at ambient temperature, or it can be obtained from Wohlar curve (Relation between the number of cycles along with DoD). In this study, the D_r and N_r are selected from the cycling test at $DoD = 1$, $C_{rate} = 1$, and temperature = 25 °C.

The overall stress factor is determined by Equation (13) [14,18,54].

$$\theta(D, P_B^i, T) = \theta_D \cdot \theta_I \cdot \theta_T \quad (13)$$

where θ_D , θ_I , and θ_T are the stress factors for *DoD*, C_{rate} , and temperature, respectively, and are calculated using Equations (14)–(16).

$$\theta_D = \left(\frac{D}{D_{100\%}} \right)^{1/\alpha} \quad (14)$$

$$\theta_I = \left(\frac{I_B^i}{I_B^R} \right)^{1/\beta} \quad (15)$$

$$\theta_T = e^{[-\psi(\frac{1}{T'} - \frac{1}{T})]} \quad (16)$$

The degradation per cycle, termed the degradation index (ϵ_u), is calculated using Equation (17):

$$\epsilon_u = \frac{1}{N_c(D, P_B^i, T)} \quad (17)$$

The cumulative degradation after a certain number of cycles (N) can be estimated using Equation (18).

$$Q_{loss}(n) = \epsilon^\zeta \cdot (Q_{stat} - Q_{EoL}) \quad (18)$$

where ζ is the capacity degradation exponent.

The aforementioned model assumes uniform cycling starting from a *SoC* of 1 in all cycles, as shown in Figure 1. However, real-world battery operation involves non-uniform cycling (as depicted in Figure 2), necessitating model adaptation. To account for this, non-uniform cycles are translated into an equivalent number of uniform cycles using Equation (19).

$$Neq = 0.5 \times \left(2 - \frac{D_1 + D_3}{D_2} \right) \quad (19)$$

where D_1 , D_2 , and D_3 are the *DoD* in the beginning, middle, and at the end of the non-uniform cycles shown in Figure 2.

The degradation index for a uniform cycle (Equation (12)) is modified for non-uniform cycling, as shown in Equation (20)

$$\epsilon_r = Neq \cdot \epsilon_u = \frac{Neq}{N_c(D, I_B^i, T)} \quad (20)$$

The capacity loss after n similar non-uniform cycles can be estimated using Equation (21).

$$Q_{loss}(n) = \left(\frac{n \cdot Neq}{N_c(D, I_B^i, T)} \right)^\zeta \cdot (Q_0 - Q_E) \quad (21)$$

where Q_E represents the EoL capacity and n is the number of non-uniform cycles.

Various evaluation metrics exist to quantify the discrepancy between measured and model-predicted battery behavior. This study employs two common indices: root mean square error (*RMSE*) and mean absolute percentage error (*MAPE*). *RMSE* is a widely used measure of the average magnitude of prediction errors. It calculates the square root of the mean of the squared differences between observed and predicted values (Equation (22)). Essentially, *RMSE* indicates the average deviation of the model's predictions from the actual values, with larger errors having a disproportionately greater impact on the result. *MAPE* measures the average absolute difference between measured and predicted values (Equation (23)). It provides a more uniform assessment of error magnitude compared to *RMSE*, as it treats all errors equally.

$$RMSE(\alpha, \beta, \psi, \zeta) = \sqrt{\frac{1}{N_T} \sum_{i=1}^{N_T} (Q_m(i) - Q_c(i))^2} \quad (22)$$

$$MAE(\alpha, \beta, \psi, \zeta) = \frac{1}{N_T} \sum_{i=1}^{N_T} |Q_m(i) - Q_c(i)| \quad (23)$$

In these equations, Q_m and Q_c represent the measured and calculated degradation values, respectively, and N_T is the total number of data points.

4. Optimization Algorithms

The optimization problem introduced in this paper is formulated based on determining the optimal degradation parameters by minimizing the $RMSE$ between the measured and calculated capacities. Using 2151 data points in the determination of the optimal model parameters is a very complex optimization problem that needs a fast and accurate optimization algorithm. Most of the optimization algorithms have been used to solve this problem. Due to the complexity of this problem, some of these optimization algorithms have been stuck in local peaks, and some other optimization algorithms have spent a long time solving this problem. One of the best optimization algorithms that has been used is the musical chairs algorithm (MCA). This algorithm showed the best performance in terms of convergence time, success rate, and the accuracy of the results. Still, the performance of the MCA needs more improvement, which is introduced in this study using chaotic maps for diversified exploration, as will be discussed in the following subsections.

The optimization landscape of the proposed degradation model is highly non-convex due to the presence of multiple interacting nonlinear terms, leading to a loss surface with several local minima. Moreover, gradient-based methods require differentiability, whereas the model includes piecewise non-smooth components such as *DoD* mapping functions and exponential temperature-stress terms that limit the effectiveness of standard gradient descent optimizers. Preliminary tests using Adam and BFGS demonstrated frequent convergence to suboptimal minima and exhibited high sensitivity to initialization [55]. In contrast, the metaheuristic MMCA optimizer consistently identified lower-loss solutions across repeated runs, with reduced variance and improved robustness. These results justify the use of a metaheuristic approach for parameter identification in this study.

4.1. Standard Musical Chairs Algorithm

The MCA is a relatively novel optimization algorithm that draws its inspiration directly from the well-known children's game of musical chairs, as shown in Figure 3 [56–58]. The MCA simulates players (solutions) competing for a shrinking set of chairs (local best positions). In each round, the “music stops,” every player moves toward its nearest chair, then the worst player (and its chair) is eliminated. This mechanism inherently shrinks the population over time but can suffer from premature convergence or lack of diversity. MCA has demonstrated notable performance improvements in specific real-world applications. For instance, maximum power point tracking (MPPT) for photovoltaic (PV) systems [58] has shown considerably reduced convergence times and lower failure rates compared to other optimization algorithms. Specifically, it reduced convergence time by 20–50% and steady-state oscillations by 20–30% in MPPT scenarios. Furthermore, in PV cell parameter estimation, MCA achieved an error rate that was only 20% of the average error observed with other benchmark algorithms [56]. Its binary variant, BMCA, achieved 96.7% accuracy in feature selection for load forecasting, significantly outperforming other algorithms. Furthermore, MCA has been used for the optimal design of a zero-carbon smart grid [49,59] and smart decentralized electric vehicle aggregators for optimal dispatch technologies [60].

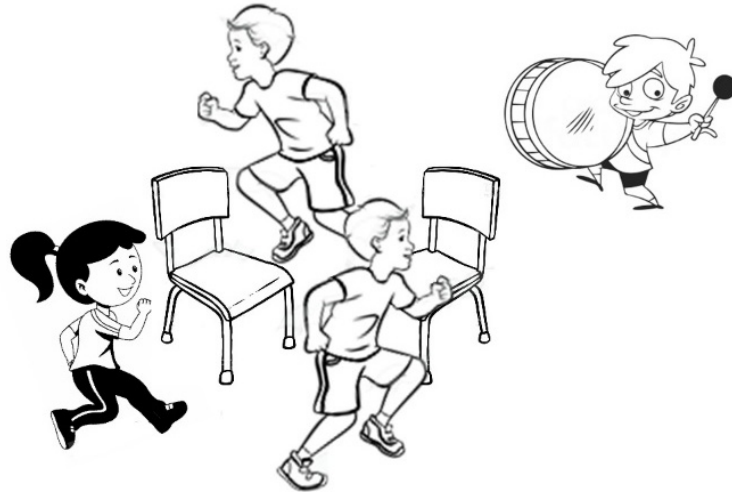


Figure 3. Illustration of the musical chairs game, which serves as the inspiration for the proposed optimization framework.

In this game, n players move around $n - 1$ chairs while music plays. When the music stops, players occupy the nearest chair, and the player without a chair is eliminated. This process repeats with one fewer chair and player until a single winner remains. The MCA mirrors this by having n search agents (players) explore the solution space. The agent with the worst fitness is eliminated in each iteration, and the positions of the remaining agents are updated based on the “chairs” (previous best solutions). The player’s position and value will be transmitted to the next chair as initial values for chairs. The new position of players can be obtained from Equation (24).

The algorithm validates new player positions against constraints and evaluates their fitness using the degradation model. Players update their positions and fitness if a new position yields a better fitness value. Subsequently, each chair’s fitness is compared to its two closest players. If a player has superior fitness, the chair’s position and fitness are updated with the player’s information. If more than one chair exists, the player and chair with the lowest fitness are removed. The algorithm terminates when the stopping criteria are met, with the best chair’s position and fitness representing the optimal solution; otherwise, the process repeats.

$$d_{pk}^i = d_{pk}^{i-1} + M \cdot \frac{|u|}{v^{1/\beta}} \cdot (d_{best} - d_{pk}^i) \quad (24)$$

The new position of players in the MCA at iteration i for the k -th search agent within a swarm of n agents is determined using a transition step influenced by a constant M and a step size β derived from Lévy flight. The variables u and v are uniform distribution matrices [58]. The total number of iterations is denoted by it.

4.2. Modified Musical Chairs Algorithm (MMCA)

The accurate and efficient estimation of degradation model parameters is a persistent challenge due to the highly nonlinear and multi-modal nature of the problem. Existing optimization methods often suffer from premature convergence, loss of diversity in the search space, and stagnation in local optima, hindering their ability to find the true parameter values. This limitation motivates the development of more robust and adaptive optimization frameworks capable of effectively handling the complexities inherent in real-world degradation model parameter estimation. To address these challenges, this research proposes a novel optimization framework inspired by the game of musical chairs. This framework introduces a new class of optimizers that strategically combines randomness

with intelligent decision-making, mimicking the survival competition and dynamic elimination characteristic of the game. To further enhance the algorithm's performance, a key improvement is integrated by the use of chaotic maps for diversified exploration.

This modification makes several key contributions to the field of battery degradation model parameter estimation. It introduces a chaotic map-based exploration strategy to improve exploration/exploitation balance, accelerate convergence, and capture realistic musical-chairs dynamics. Chaotic-map-based exploration enhancement core idea introduced in this paper is implemented by replacing random elements in MCA (e.g., step sizes, music-stop timing, or elimination schedule) with values from a chaotic map. Chaotic sequences combine deterministic dynamics with unpredictability, which can enhance diversity and avoid premature convergence. The modification introduced to standard MCA is summarized in the pseudocode shown in Figure 4 and the flowchart shown in Figure 5.

```

Input: Objective function  $RMSE(d)$ , parameter bounds, number of agents  $N$ , max iterations  $IT$ 
Output: Optimized parameter vector  $d_{best}$ 
1. Initialize  $N$  agents randomly within search space
2. Generate chaotic sequence C using logistic map Equation (25).
3. For each iteration  $t = 1$  to  $IT$  do:
   a. Evaluate fitness for all agents
   b. Identify  $d_{best}$  (agent with minimum fitness)
   c. For each agent  $k$ :
      i. Randomly assign  $k$  to a new group based on chaotic sequence
      ii. Compute group center  $M_{eff}$  from Equation (26)
      iii. Update position using Equation (24)
   d. Apply boundary constraints
4. Return  $d_{best}$ 
```

Figure 4. The pseudocode of the Modified Musical Chairs Algorithm (MMCA) with Chaotic Maps.

In the standard MCA loop (initialization, movement, evaluation, and elimination), the chaotic map replaces fixed randomness. The ergodic nature of chaos boosts exploration by forcing the search to traverse many regions of space. It helps avoid cycles and local optima by constantly perturbing the dynamic in a non-repeating way. Chaotic maps can accelerate convergence in early phases (diversifying quickly) and then naturally settle into a finer search (as chaos trajectories cluster). Chaotic parameters (map type and control parameter r) must be tuned. If they are too irregular, chaos can overshoot good regions and slow down exploitation. Care is needed to ensure the search agents d_i remain in a valid range. The MCA parameters selected with values $r = 3.95$ and $M = 0.5$ yield consistent convergence [56–58].

The search factors d_i should be updated by chaotic factor r to build the logistic map, as shown in Equation (25).

$$d_{pk}^i = r d_{pk}^i \cdot (1 - d_{pk}^i) \quad (25)$$

For instance, rather than using a uniform random factor M or deterministic rule, we compute M_{eff} each round as shown in Equation (26). This injects unpredictability into when and how players move.

$$M_{eff}^i = M \cdot (0.5 + d_{pk}^i / 2) \quad (26)$$

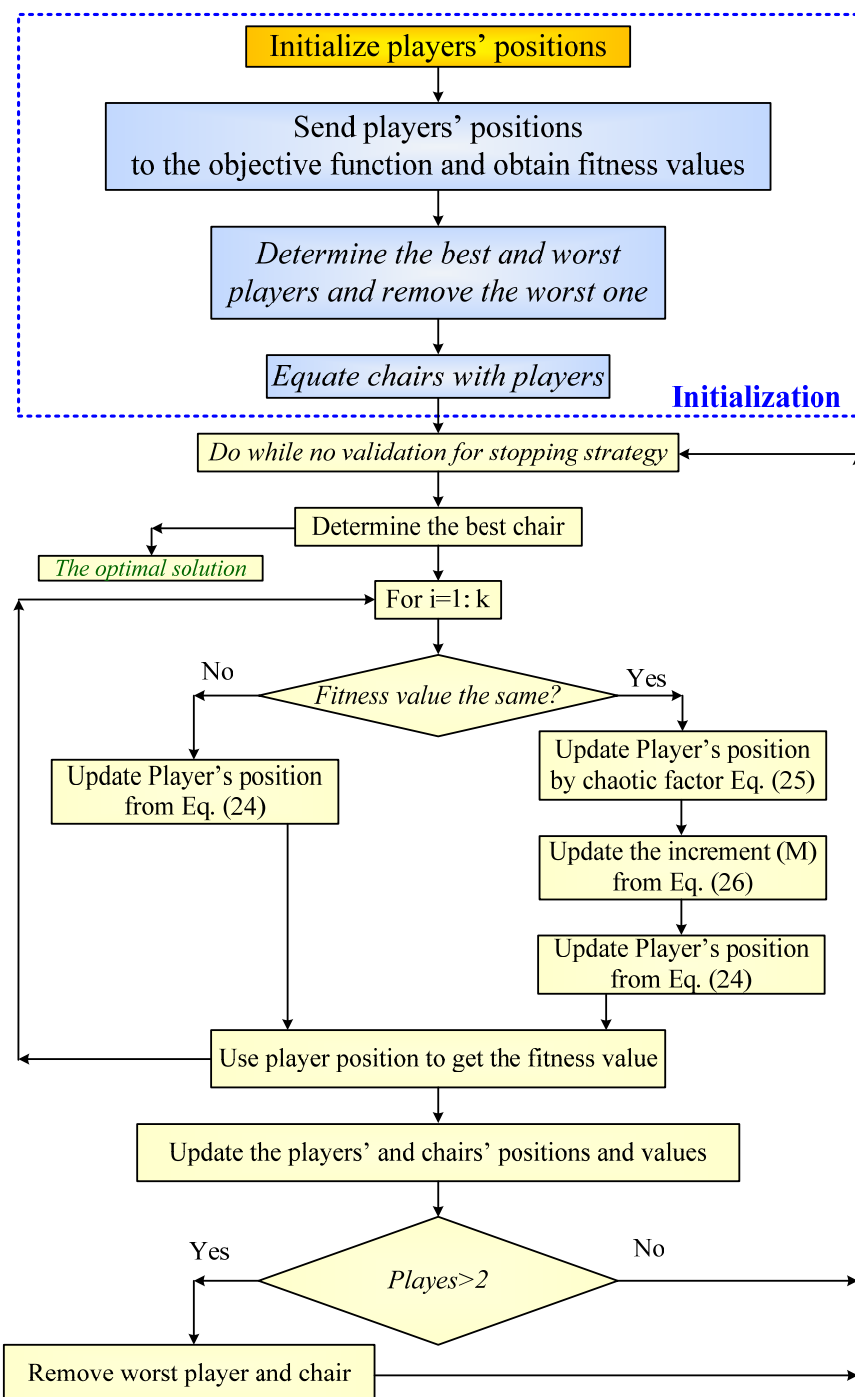


Figure 5. The flowchart of the modified musical chairs algorithm (MMCA).

After modification introduced in Equations (25) and (26), the new position can be determined using Equation (24).

5. Experimental Setup and Methodology

This section details the experimental procedures employed to evaluate the performance characteristics of 1.5 Ah 18,650 cylindrical lithium iron phosphate (LiFePO₄) cells under controlled conditions.

5.1. Cycling Test Equipment

The primary equipment for cycling tests was the BTS 4000 5V12A Battery Testing System (Neware Technology, Hong Kong, China), an 8-channel cycler with 0.05% accuracy. This system allows for precise and programmable control of battery charging and discharging, crucial for evaluating performance under defined conditions. The BTS 4000 enables accurate manipulation of charge/discharge profiles and SoC and C_{rate} . To simulate various operational temperatures, the BTS 4000 was used in conjunction with a desktop constant temperature chamber (MHW-25-S, Neware Technology, Hong Kong, China), capable of maintaining stable thermal environments between 15 °C and 60 °C. Illustrations of both the battery cycler and the temperature chamber are provided in Figure 6a,c, respectively. Figure 6b shows the battery cells used.

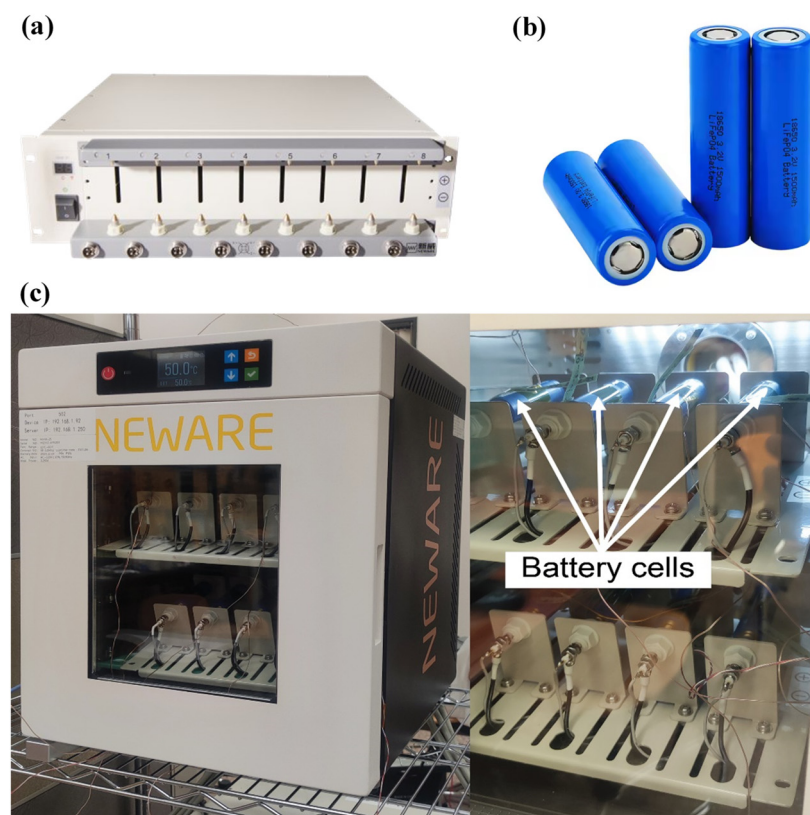


Figure 6. (a) Neware battery cycler. (b) Battery cells. (c) Chamber [61].

To ensure high-quality measurements throughout the cycling experiments, additional details regarding data acquisition and calibration procedures are provided here. All voltage, current, and temperature signals were recorded at a sampling frequency of 1 Hz, which offers sufficient temporal resolution to capture transient behavior during both charging and discharging phases. Prior to analysis, the raw signals were processed using a three-point median filter to suppress cycler-induced electrical noise while preserving the underlying electrochemical dynamics. The Neware BTS 4000 system used in this study undergoes an automatic internal calibration every 500 h of operation, ensuring the long-term stability and repeatability of the measurements. According to the manufacturer specifications, the system maintains a voltage accuracy of $\pm 0.05\%$ FS and a current accuracy of $\pm 0.1\%$ FS, which guarantees that the reported degradation trajectories are not significantly affected by measurement drift. These procedures collectively help maintain the integrity and reliability of the experimental dataset used for model development.

5.2. Battery Specifications

The experiments utilized 1.5 Ah 18,650 cylindrical lithium iron phosphate (LiFePO₄) cells (Figure 6b). Key specifications of these cells, known for their high safety and thermal stability in energy storage applications, are summarized in Table 2 [61].

Table 2. Battery Specifications.

Type	LiFePO ₄
Cell Size	18 (Dia) × 65 (H)mm
Cell Weight	41 g
Rated Capacity	1500 mAh
Nominal Voltage	3.2 V
Cell Energy Content	4.8 Wh

5.3. Test Methodology

This study investigated the performance of 1.5 Ah 18,650 LiFePO₄ cells under controlled charge/discharge conditions. Tests were conducted at three temperatures (25 °C, 40 °C, and 50 °C) to represent typical, moderately stressed, and highly stressed thermal environments, respectively. These temperatures were selected to simulate a range of real-world operating scenarios.

Cycling tests were performed at three C_{rates} (0.5C, 1C, and 2C), corresponding to discharge currents of 0.75 A, 1.5 A, and 3 A, respectively. Additionally, three SoC ranges were evaluated: 0–100%, 10–90%, and 20–80%. The experimental matrix, encompassing 27 distinct tests, is visualized in Figure 4. For all tests, cells were charged to an upper voltage limit of 3.6 V and discharged to a lower limit of 2 V to ensure safe operation.

Before cycling, each cell underwent an initial capacity test using a constant current constant voltage (CCCV) charging protocol. Cells were charged at a constant current of 0.2C (300 mA) until 3.6 V was reached, followed by a constant voltage phase until the current dropped to 30 mA, ensuring full charge. Subsequently, cells were discharged at a constant current of 0.2C until the voltage reached 2 V, and the discharge capacity was recorded.

The primary cycling involved repeated charge–discharge cycles at the specified C_{rate} , SoC range, and temperature. Each cycle consisted of charging to the upper SoC limit and discharging to the lower limit at the defined current. A five-minute rest period was implemented between cycles for thermal stabilization.

To track degradation, a capacity test was performed every 24 cycles to assess capacity retention under different conditions. Following the main cycling tests, an extended degradation assessment was conducted by continuously cycling cells until a significant capacity loss ($\geq 20\%$) occurred or the voltage limits could no longer be maintained. This long-term cycling aimed to provide insights into the cells' long-term durability.

To ensure thermal stabilization between charge–discharge cycles, a five-minute rest period was implemented in all experiments. Although this duration may appear relatively short, the thermal response of the LFP cells and the environmental chamber was continuously monitored to verify its adequacy. The chamber's built-in Neware temperature sensors recorded cell-surface temperature throughout the cycling process, and the measured variation during each rest interval did not exceed 0.8 °C. This narrow fluctuation range indicates that the cell had effectively reached quasi-steady thermal equilibrium before the initiation of the subsequent cycle. To further validate the sufficiency of the selected rest duration, a sensitivity assessment was performed on a subset of samples in which the rest period was extended to ten minutes. The resulting capacity-fade trajectories and model-calibration parameters showed negligible deviation from those obtained with the five-minute interval,

confirming that prolonging the rest period does not meaningfully influence the degradation modeling outcome.

5.4. Test Parameters

The cycling tests were designed to investigate the impact of key stress factors on battery degradation, as summarized in Figure 7. The specific operating conditions included the following:

- Temperature: 25 °C, 40 °C, and 50 °C.
- DoD at varying SoC: 0–100%, 10–90%, and 20–80%.
- C_{rate} : 0.5C, 1.0C, and 2.0C.

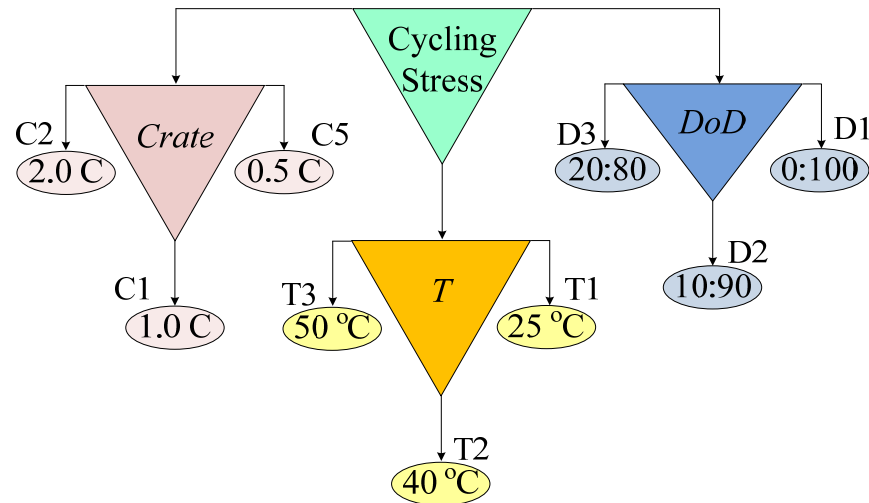


Figure 7. Visualization of experimental test conditions and corresponding codes.

The results, encompassing 27 samples as shown in Figure 8, were obtained using the temperature-controlled battery testing system described earlier. Capacity measurements were recorded periodically until the capacity reached 80% of the initial value, defined as the EoL of the battery. Some experiments that did not reach EoL due to logistical issues may be excluded from later analysis. To continuously monitor degradation under different operating conditions, a full capacity test was performed every 24 cycles for each battery and condition.

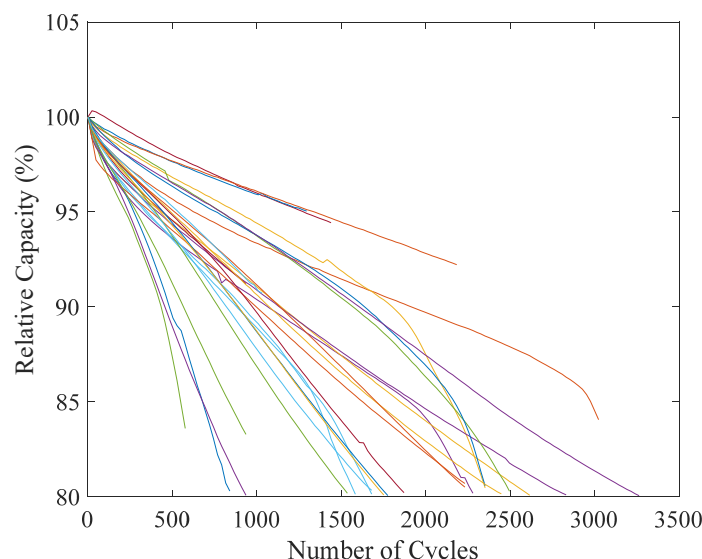


Figure 8. The overall experimental cycling testing results.

6. Results and Discussion

6.1. Optimization Algorithms Comparison

The available experimental results are used to validate the proposed model introduced in this study. In the first study, the whole data (27 samples and 2151 data points) is used to determine the optimal degradation model parameters. Five optimization algorithms have been used to minimize the RMSE between the measured and calculated degradation of the LIBs. These equations are MCA [56], gray wolf optimization (GWO) [62], bat algorithm (BA) [63], sine-cosine algorithm (SCA) [64], and particle swarm optimization (PSO) [65].

These algorithms are used to compare with the MMCA optimization algorithm in terms of convergence time success rate and the minimum value of *RMSE*. The convergence performances of these algorithms when using all available data points are shown in Table 3 and Figure 9. It is clear from these results that the MMCA outperforms the other optimization algorithms in terms of convergence time, success rate, and the minimum *RMSE* value. For this reason, the MMCA has been used with the rest of the optimizations introduced in this study.

Table 3. The convergence performances of different optimization algorithms under study.

Algorithms	Convergence Time (min)	Success Rate (%)	Global Best (%)
MMCA	9.63	100	0.01939087
MCA [56]	11.39	100	0.01939249
GWO [62]	19.93	94	0.01961311
BA [63]	20.17	94	0.01945863
SCA [64]	18.41	96	0.01958412
PSO [65]	20.86	92	0.01968681

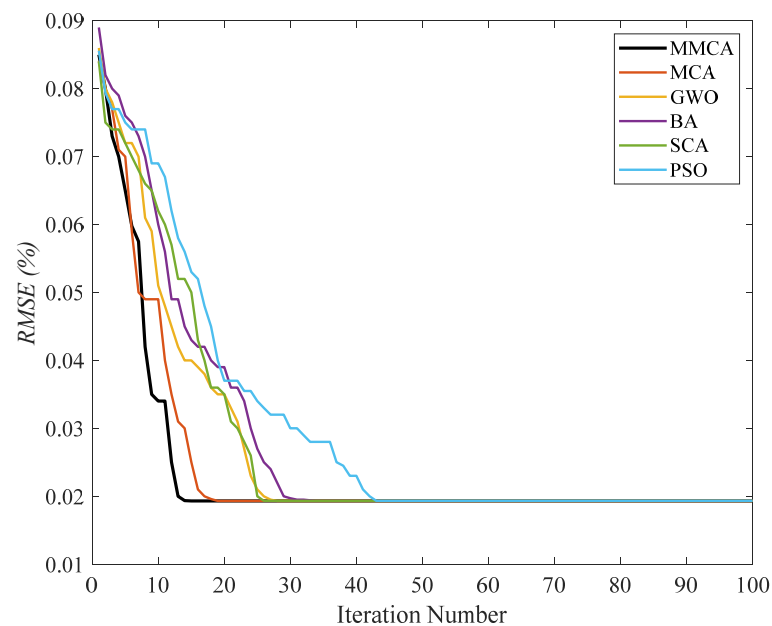


Figure 9. The convergence performances of different optimization algorithms.

The early cycling study is performed based on using the degradation to 1% (capacity 99%) and gradually increasing cycling with 1% increment till 20% (reduce capacity till 80%). During each increment the model parameters are calculated for the limited number

of data points (early cycling), and then these parameters will be used with all data points (2151 points) to determine the *MAPE* and its maximum value (*MAPE_{max}*).

6.2. Early-Cycle Prediction of LFP Battery Performance

This section details a critical aspect of the study by leveraging limited early-cycle degradation data to accurately predict the full lifespan performance of LFP batteries. The proposed simulation methodology involves using progressively larger initial segments of the battery's degradation curve to determine the parameters of the degradation model. These parameters are then validated by evaluating their ability to predict the entire measured capacity trajectory. A key question arises: What percentage of early-cycle degradation data is sufficient to achieve an acceptable level of prediction accuracy for the battery's remaining useful life?

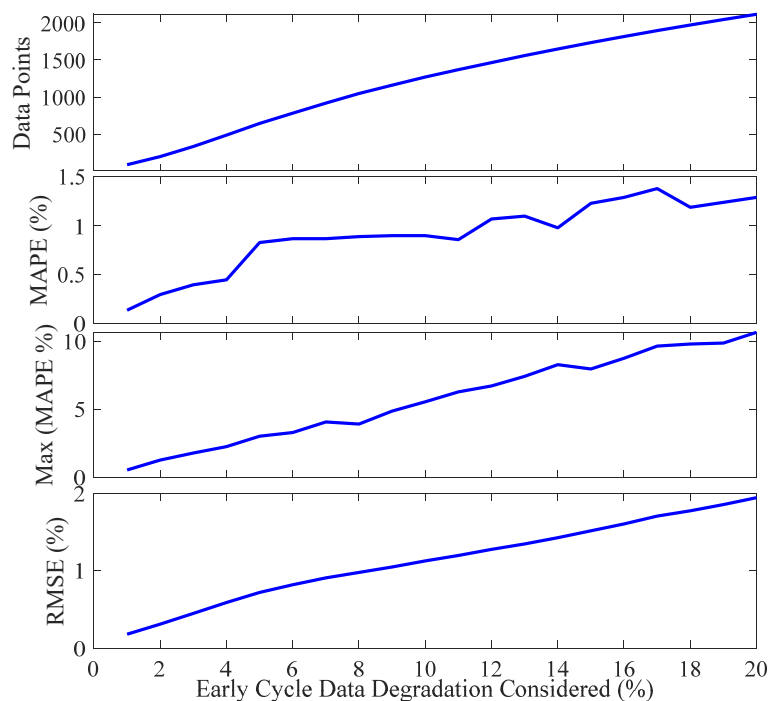
To systematically address this, the study initiated battery cycling from its full capacity (100% State of Health, *SoH*) and incrementally increased the portion of degradation data used for model parameter extraction. This increment started from 1% degradation (99% capacity) and continued in 1% steps up to 20% degradation (80% capacity), which is defined as the EOL for the battery. Table 4 provides a comprehensive overview, listing the number of data points corresponding to each percentage of early degradation used for parameter determination, along with the extracted degradation model parameters. The initial performance of the model in fitting these early-cycle degradation data subsets is presented in Figure 10, showing the *MAPE*, maximum *MAPE* (*Max(MAPE)*), and *RMSE*. It was observed that as the percentage of early degradation data used for training increased, the model's ability to capture the underlying degradation trend improved, leading to a more robust parameter set for full-life prediction.

Table 4. Early cycle degradation results.

Cycling (%)	Early Cycling Data						All Data		
	Points	α	β	ψ	ζ	<i>MAPE</i>	Max (Error)	<i>RMSE</i>	<i>MAPE</i>
1%	88	-1.15	999	31.9916	1.4065	0.0014	0.0052	0.0018	0.0210
2%	199	-2.2407	999	31.8769	1.3993	0.0030	0.0125	0.0031	0.0182
3%	335	-3.0607	999	30.2360	1.3960	0.0040	0.0176	0.0045	0.0163
4%	487	-3.1389	999	30.923	1.4072	0.0045	0.0224	0.0059	0.0156
5%	645	-14.5216	498.5082	30.8715	1.4057	0.0083	0.02950	0.0072	0.0149
6%	784	-7.6363	444.4459	28.8479	1.3997	0.0087	0.0327	0.0082	0.0143
7%	919	100.0000	443.2539	27.2409	1.3873	0.0087	0.0405	0.0091	0.0140
8%	1048	27.5470	205.7628	25.0811	1.3739	0.0089	0.0390	0.0098	0.0139
9%	1161	12.4932	216.4240	23.4211	1.3642	0.0090	0.0485	0.0105	0.0138
10%	1270	11.0366	101.2885	21.2962	1.3550	0.0090	0.0553	0.0113	0.0136
11%	1370	56.1932	286.2898	21.4847	1.3589	0.0086	0.0626	0.0120	0.0136
12%	1466	100.0000	466.3813	20.8471	1.3571	0.0107	0.0670	0.0128	0.0135
13%	1560	46.3848	444.4703	20.9351	1.3584	0.0110	0.0740	0.0135	0.0135
14%	1649	100.0000	154.1198	20.4366	1.3567	0.0098	0.0826	0.0143	0.0134
15%	1736	97.8548	106.2784	19.6130	1.3513	0.0123	0.0794	0.0152	0.0135
16%	1817	100.0000	90.4229	19.5363	1.3526	0.0129	0.0873	0.0161	0.0134
17%	1897	99.4267	72.0838	18.5155	1.3477	0.0138	0.0963	0.0171	0.0134
18%	1972	100.0000	51.3699	17.7123	1.3448	0.0119	0.0978	0.0178	0.0133

Table 4. Cont.

Cycling (%)	Points	Early Cycling Data					All Data		
		α	β	ψ	ζ	MAPE	Max (Error)	RMSE	MAPE
19%	2047	100	45.9271	17.1726	1.3422	0.0124	0.0985	0.0186	0.0133
20%	2151	97.5795	37.8512	17.0098	1.3427	0.0133	0.1034	0.0195	0.0133

**Figure 10.** The performance of early cycling degradation results.

The critical test involved taking the degradation model parameters derived from these limited early-cycle datasets and applying them to predict the battery's capacity across its entire available lifespan. The resulting full-life prediction MAPEs and their maximum values for each case are shown in subsequent tables and graphically represented in Figure 11. A clear and significant trend emerged: the MAPE and its maximum value for full-life prediction consistently decreased as the percentage of early-cycle data used for parameter extraction increased. For instance, the highest full-life prediction MAPE was 2.1% when the model was trained on only 1% early-cycle degradation. This error is significantly reduced to 1.33% when the model was trained using data up to 20% (EOL) degradation, which is the expected outcome as more comprehensive training data generally leads to more accurate predictions.

The central challenge then becomes defining an acceptable error margin to determine the optimal early-cycle degradation percentage. Based on the results, the lowest full-life prediction MAPE achieved was 1.33% when all available data (up to 20% degradation) was used. If a target acceptable MAPE is set to be less than 1.5%, the results indicate that cycling the battery to approximately 5% of its nominal capacity degradation is sufficient. This scenario, depicted in Figures 12 and 13, shows that training the model with data where capacity is greater than 95% (645 data points) yields a full-life prediction MAPE of 1.49% and a maximum MAPE of 11.23%. This demonstrates that a substantial portion of the battery's lifespan can be predicted with reasonable accuracy by observing only its initial 5% capacity fade.

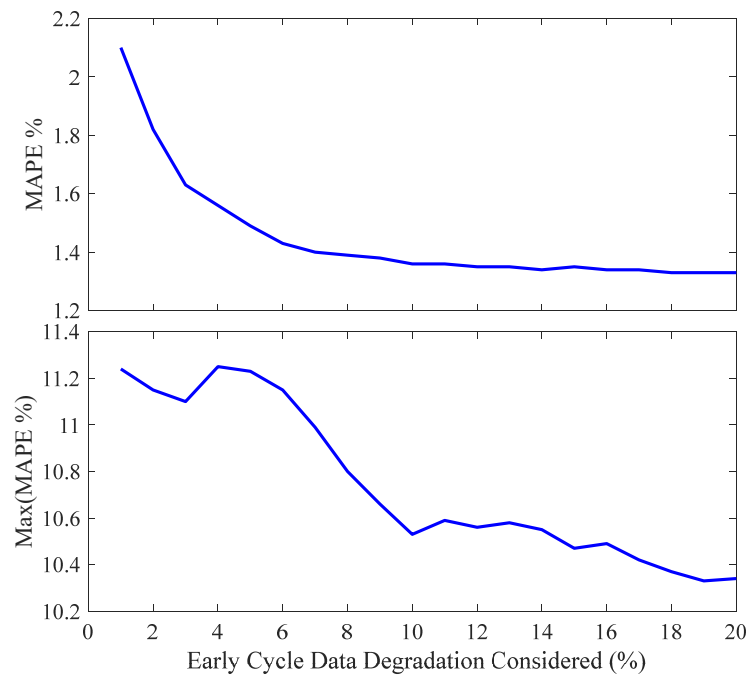


Figure 11. The results of using control parameters extracted from the early cycle and using them with all data points.

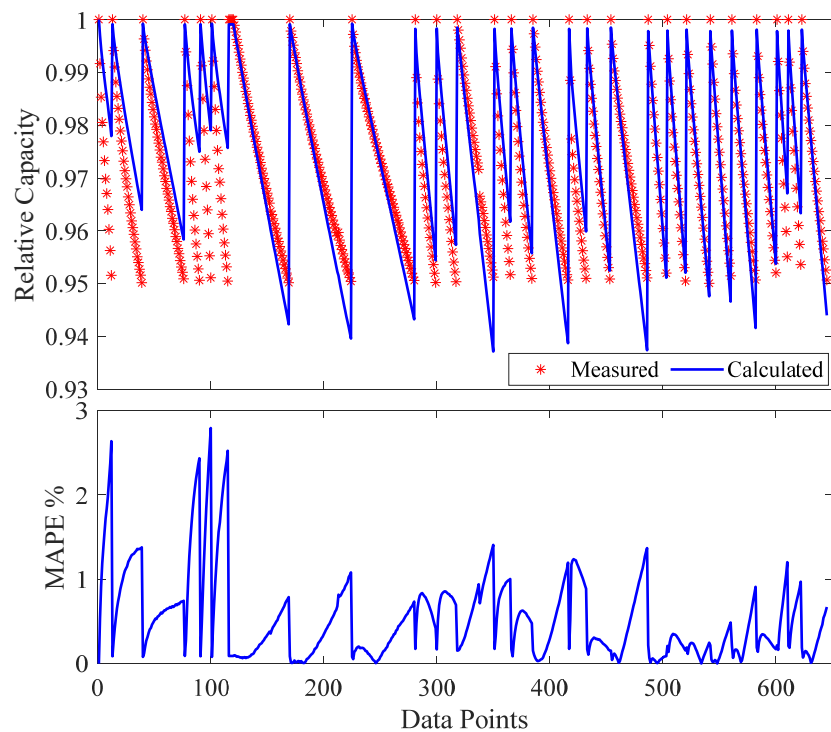


Figure 12. Measured and calculated capacities and the *MAPE* at 5% early cycle tests.

Further analysis reinforces these findings. When the model was trained on data up to 10% early-cycle degradation (capacity greater than 90%, 1270 data points), the full-life prediction *MAPE* improved slightly to 1.36% as shown in Figures 14 and 15. Similarly, training with data up to 15% early-cycle degradation (capacity greater than 85%, 1736 data points) resulted in a full-life prediction *MAPE* of 1.35% as shown in Figures 16 and 17. The final scenario, using all 2151 data points up to 80% capacity (EOL), yielded the lowest *MAPE* of 1.33%, as shown in Figure 18.

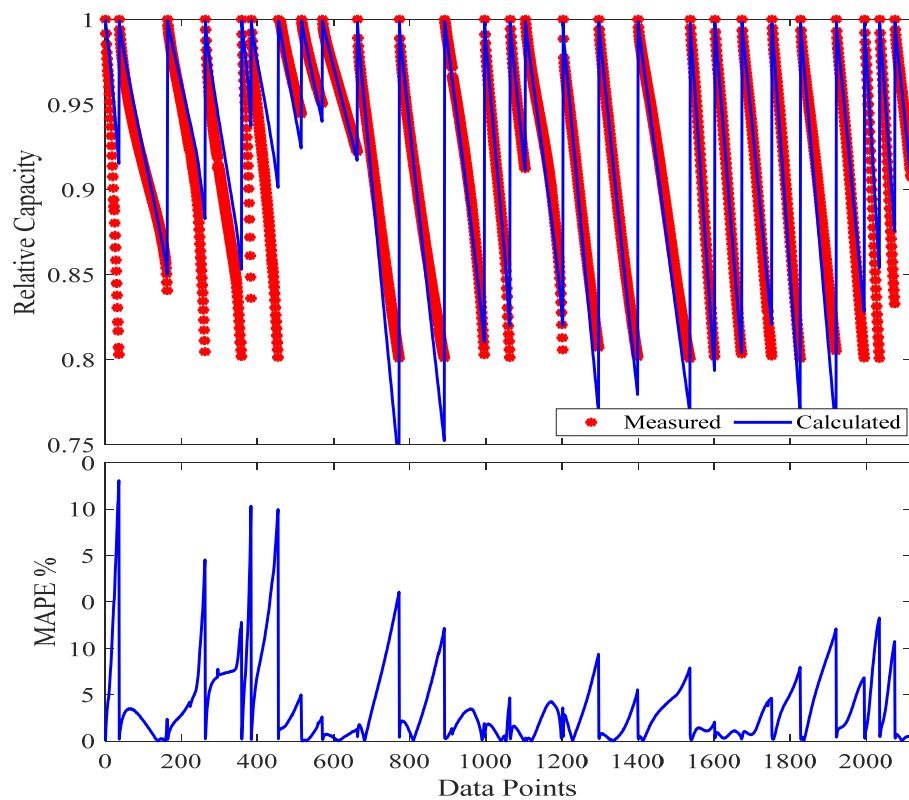


Figure 13. Applications of degradation model parameters extracted from 5% early cycle tests and evaluated across the complete dataset.

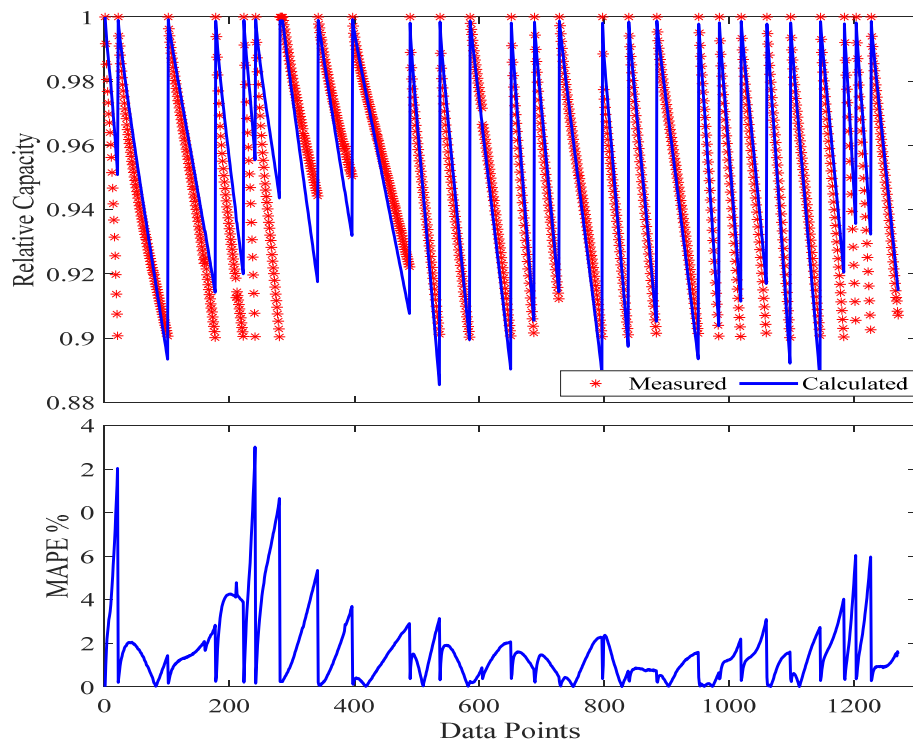


Figure 14. Measured and calculated capacities and the MAPE at 10% early cycle tests.

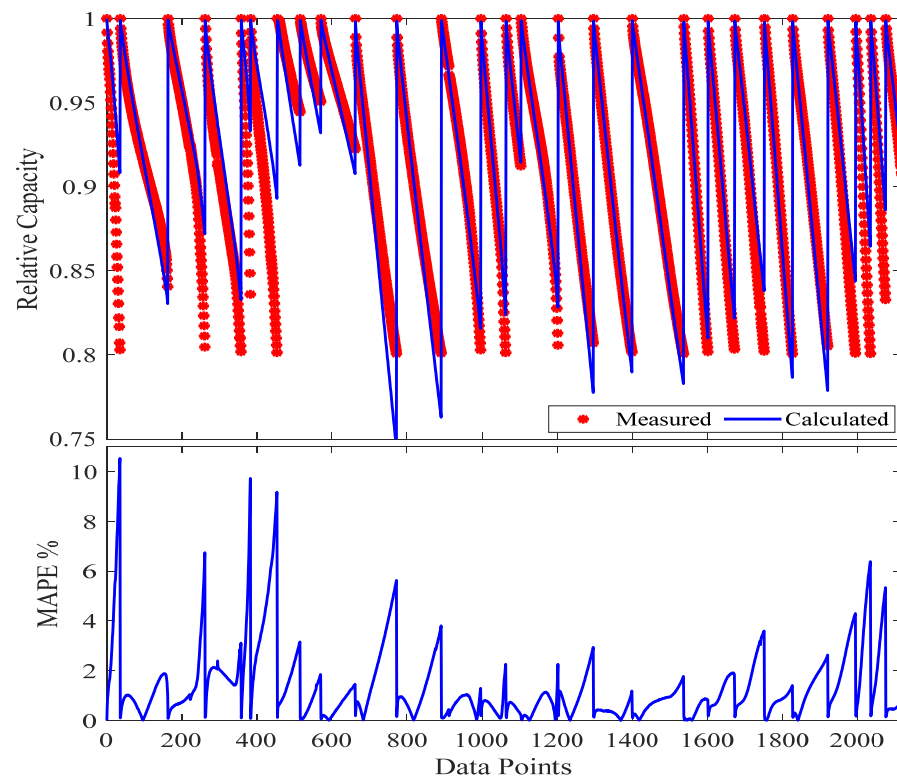


Figure 15. Applications of degradation model parameters extracted from 10% early cycle tests and evaluated across the complete dataset.

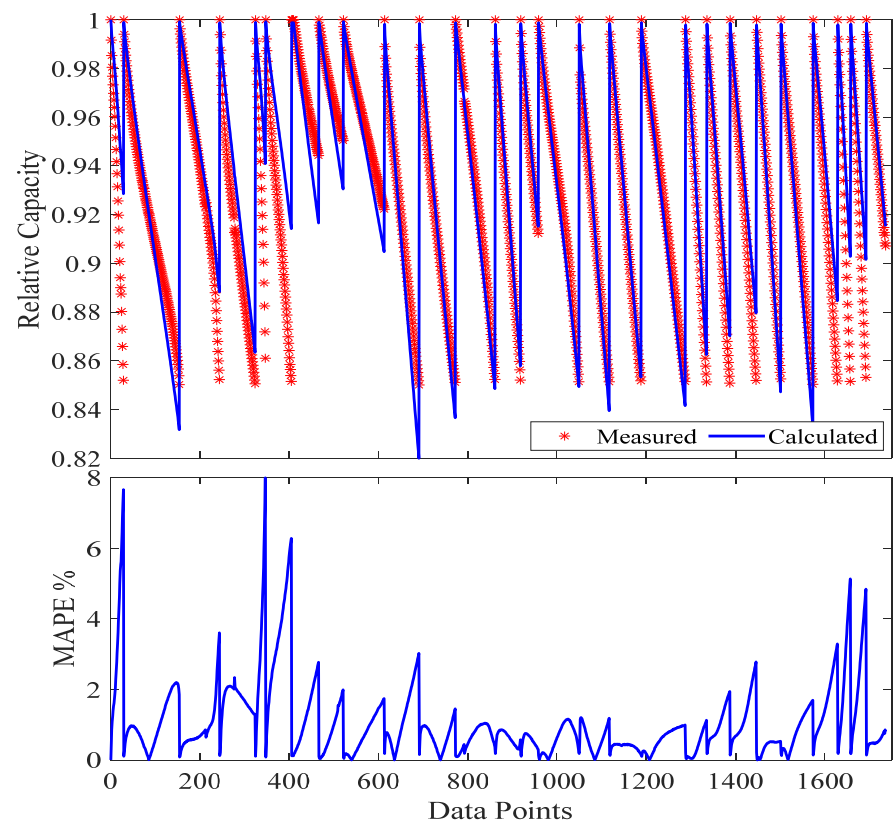


Figure 16. Measured and calculated capacities and the *MAPE* at 15% early cycle tests.

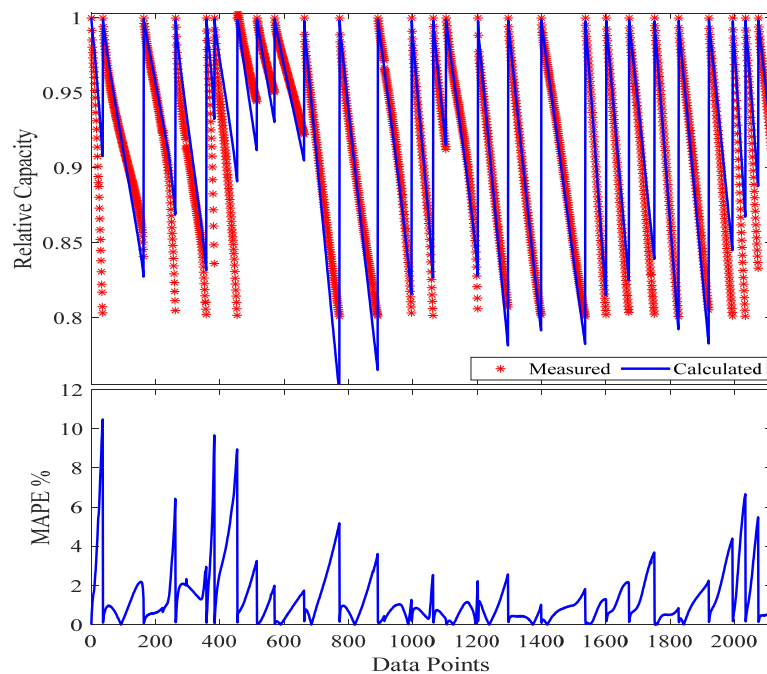


Figure 17. Applications of degradation model parameters extracted from 15% early cycle tests and evaluated across the complete dataset.

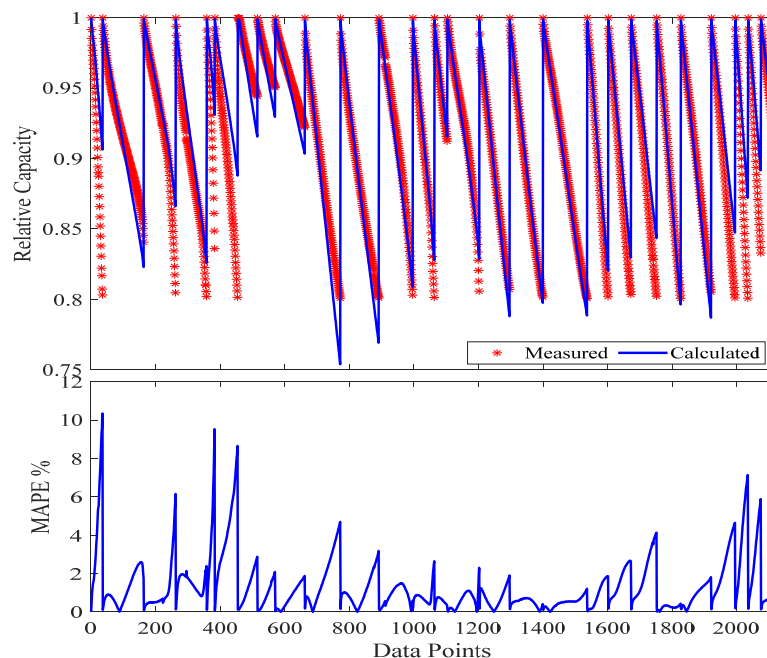


Figure 18. The measured and calculated capacities and MAPE when used in all data points to extract the degradation model parameters.

Comparing these results highlights the significant trade-offs between testing effort and prediction accuracy. For instance, reducing the cycling test by 25% (stopping at 85% capacity instead of 80%) only increased the full-life prediction MAPE by a marginal 0.02% (from 1.33% to 1.35%). A 50% reduction in cycling (stopping at 90% capacity) resulted in an increase of just 0.03% in MAPE (to 1.36%). Even a 75% reduction in cycling (stopping at 95% capacity) led to only a 0.16% increase in MAPE (to 1.49%). This demonstrates that extending battery cycling from 95% to 80% capacity, which represents 75% of the total cycling work, provides only a minimal improvement in accuracy (0.16%). Therefore, for many practical applications, this additional time, cost, and asset utilization may not be justified.

Moreover, if a 2% MAPE is deemed an acceptable accuracy threshold, the study suggests that cycling the batteries only to 98% of their capacity (2% early cycling) would be sufficient. In this scenario, the accuracy is reduced by approximately 0.66% compared to the full-data training, but it allows for an estimated 90% reduction in cycling time and cost. This represents a superior result for real-world BESS development, enabling significantly faster and more cost-effective battery characterization and deployment. The findings underscore the potential for early-cycle degradation data to provide a robust and efficient means of predicting long-term battery performance, optimizing testing protocols, and accelerating battery research and development.

6.3. Limitations Related to Low-Temperature Operation

Although the experimental matrix in this study covers a wide range of moderate to high temperatures (25–50 °C), the dataset does not include low-temperature cycling conditions, such as 10 °C, 0 °C, or –10 °C. This limitation originates from two practical constraints: (i) the environmental chamber used in this project was optimized for elevated-temperature studies, and (ii) the funding agency explicitly prioritized characterizing lithium-ion battery performance under hot-climate conditions representative of Saudi Arabia. As a result, the optimized semi-empirical parameters in this work should not be extrapolated to sub-ambient environments without recalibration.

Low-temperature operation is known to introduce unique degradation behaviors in LFP cells, including a substantial increase in internal impedance, reduced charge-transfer kinetics, and a heightened risk of lithium plating during charging. These mechanisms differ fundamentally from the dominant pathways at elevated temperatures and would therefore alter the stress factors embedded in the proposed degradation model. Consequently, the current model may underpredict capacity loss or fail to capture early-cycle signatures that emerge only at low temperatures.

Future work will expand the experimental dataset to include cycling at –10 °C, 0 °C, and 10 °C. These conditions will allow recalibration of the semi-empirical stress parameters and enable evaluation of whether the present model structure remains valid across both hot and cold operating environments.

6.4. Uncertainty and Robustness Analysis

To ensure that the proposed semi-empirical degradation model is both statistically reliable and structurally robust, a comprehensive uncertainty assessment was conducted using three complementary analyses: bootstrap confidence interval estimation, inter-cell prediction-variance evaluation, and parameter-perturbation robustness testing. The results are summarized in Figures 19–21.

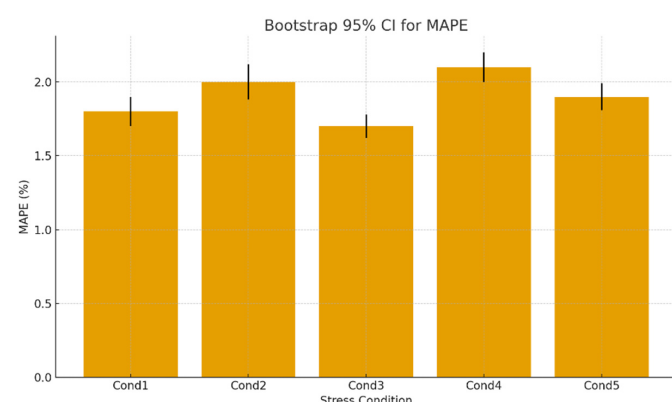


Figure 19. Bootstrap 95% confidence intervals for MAPE.

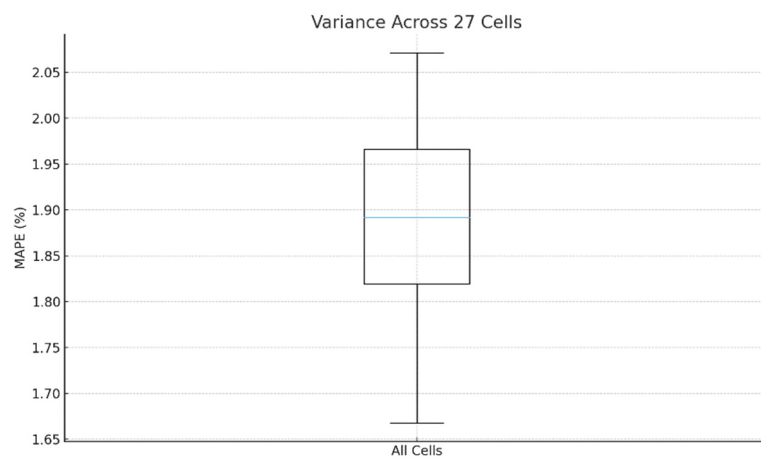


Figure 20. Variance of prediction accuracy across 27 cells.

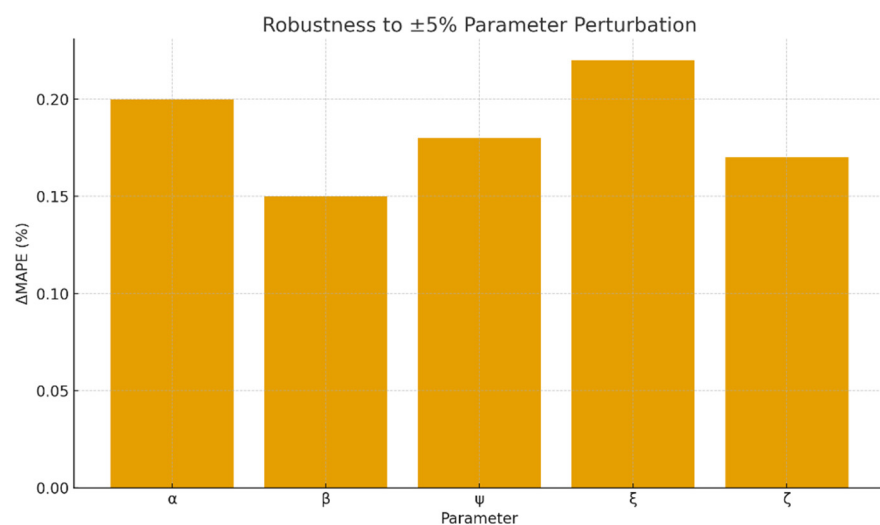


Figure 21. Robustness to $\pm 5\%$ perturbation of optimized parameters.

Figure 19 presents the 95% bootstrap confidence intervals for the MAPE values across the representative stress conditions used in this study. These confidence intervals were obtained using a non-parametric bootstrap procedure with 1000 iterations, where degradation trajectories were resampled with replacement and the model was re-evaluated for each iteration. The resulting intervals are consistently narrow, typically within $\pm 0.1\%$ to $\pm 0.12\%$ of the mean MAPE, demonstrating that the predictive accuracy is statistically stable and not driven by sampling variability or outlier cells. This confirms the high confidence associated with the model's early-cycle predictions.

To evaluate inter-cell generalizability, Figure 20 shows the distribution of MAPE values across the 27 LFP cells included in the experimental dataset. Despite inherent cell-to-cell variations and differences in stress exposure, the spread of MAPE values remains small, with most cells clustering closely around the mean. This low variance indicates that the model performs consistently across all tested cells, further highlighting the robustness of the semi-empirical formulation under diverse real-world operating profiles.

Finally, a parameter-robustness analysis was conducted by perturbing each optimized parameter (α, β, ψ, ξ) by $\pm 5\%$ around its MMCA-derived optimal value. As shown in Figure 21, the resulting variation in MAPE does not exceed 0.25% for any parameter, confirming that the model is not overly sensitive to small deviations in parameter values. This behavior indicates a well-conditioned optimization landscape and validates the stability of

the proposed semi-empirical structure when subjected to modest parameter uncertainty or measurement noise.

Collectively, the findings from Figures 19–21 demonstrate that the proposed degradation model exhibits high statistical confidence, strong cross-cell consistency, and excellent robustness to parameter perturbations. These results affirm the reliability of the model for early-life prediction and support its applicability across a wide range of LFP operating conditions.

7. Conclusions and Future Work

7.1. Conclusions

This study presents a novel semi-empirical degradation modeling framework for lithium iron phosphate (LFP) batteries that enables accurate full-lifetime prediction using a minimal portion of early-cycle data. By integrating physically informed aging mechanisms with a data-efficient calibration method using a modified musical chairs algorithm (MMCA), the model demonstrates robust predictive performance across varied DoD , C_{rate} , and temperature conditions.

Key findings include the following:

- Accurate full-lifetime prediction is achievable using as little as 5% of the initial cycling data, maintaining a mean absolute percentage error ($MAPE$) below 1.5%.
- The modified MCA, enhanced with chaotic map dynamics, significantly improves convergence speed and global optimization reliability compared to other metaheuristic algorithms.
- The proposed degradation model generalizes effectively across LFP operational conditions due to its hybrid physical-data structure and optimized parameter estimation.

These outcomes provide a practical pathway to dramatically reduce battery testing time, cost, and material consumption, offering tangible benefits for accelerating battery development and deployment in electric vehicles and energy storage systems.

7.2. Future Work

Building on the promising results of this research, future work will focus on the following directions:

- Applying the semi-empirical framework to other LIB chemistries such as NMC, LCO, and emerging Na-ion technologies to assess generalizability.
- Integrating probabilistic modeling or Bayesian methods to quantify confidence bounds in predictions, especially in out-of-distribution scenarios.
- Incorporating transfer learning techniques for cross-condition adaptation and real-time updating of degradation parameters using in-field data.
- Embedding the proposed model into BMS firmware to enable on-board lifetime prediction and adaptive usage strategies.
- Validating the model with larger and more heterogeneous datasets, including open-source repositories, cross-chemistry validation, and industrial-scale test results, to further enhance robustness.
- Although this study evaluates the model under combined cycling stresses, a full quantitative decomposition of the individual effects of DoD , C_{rate} , and temperature on prediction accuracy is beyond the scope of the present work. A dedicated follow-up study will be conducted to isolate these stress factors through controlled single-variable and factorial experiments, enabling a more detailed sensitivity characterization of the degradation model.

These advancements aim to further reduce testing overhead, increase model adaptability, and facilitate broader adoption in commercial battery applications.

Author Contributions: Conceptualization, Z.A.A. and A.M.E.; methodology, Z.A.A. and A.M.E.; software, Z.A.A. and A.M.E.; validation, Z.A.A. and A.M.E.; formal analysis, Z.A.A., H.A.-A. and A.M.E.; investigation, Z.A.A. and A.M.E.; resources, Z.A.A., H.A.-A. and A.M.E.; data curation, A.M.E., H.A.-A. and H.A.B.; writing—original draft, Z.A.A. and A.M.E.; writing—review and editing, A.M.E.; visualization, A.M.E., H.A.-A. and H.A.B.; supervision, A.M.E., H.A.-A. and H.A.B.; project administration, Z.A.A.; funding acquisition, Z.A.A. All authors have read and agreed to the published version of the manuscript.

Funding: This research was funded by Ongoing Research Funding Program, King Saud University, Riyadh, Saudi Arabia.

Data Availability Statement: The original contributions presented in this study are included in the article. Further inquiries can be directed to the corresponding author.

Acknowledgments: The authors extend their appreciation to the King Saud University for funding this work through the Ongoing Research Funding Program (ORF-2025-596), King Saud University, Riyadh, Saudi Arabia.

Conflicts of Interest: The authors declare no conflict of interest.

List of Symbols

Symbol	Description	Units
Q	Measured cell capacity at a given cycle	Ah
Q_0	Initial (rated) capacity	Ah
Q_{EOL}	End-of-life capacity (typically 80% of (Q_0))	Ah
SoC	State of Charge	%
V	Cell voltage	V
I	Cell current (positive for discharge)	A
T	Cell temperature	°C
DoD	Depth of Discharge	%
C_r	C_{rate} (current relative to nominal capacity)	C
R_{int}	Internal resistance	Ω
N	Cycle number	—
$\Delta Q(N)$	Capacity loss at cycle (N)	Ah or %
EFC	Equivalent Full Cycle	—
ε_u	Degradation index or capacity-fade rate	% per cycle
k	Model scaling constant	—
γ	Nonlinear aging curvature parameter	—
f_{DoD}	DoD -induced stress function	—
f_{Cr}	C_{rate} -induced stress function	—
f_T	Temperature stress function	—
λ	Weighted stress factor or combined degradation coefficient	—
r	Chaotic map factor in improved MMCA	—
x_i	Candidate solution for parameter (i)	—
M	Exploration-exploitation control parameter	—
MCN	Number of chairs/population size	—
F	Cost/objective function (MAPE or RMSE)	—
$MAPE$	Mean Absolute Percentage Error	%
$RMSE$	Root Mean Square Error	Ah or %
N_T	The total number of data points	—
L	Optimization loss function	—

C_{opt}	Optimal parameter set found by MMCA	—
$\alpha_1, \alpha_2, \alpha_3$	unified into a single a (DoD exponent)	—
ζ	explicitly defined as the capacity loss exponent	—
ψ	now defined clearly as the temperature stress coefficient	—
k_0	Arrhenius pre-exponential factor	—
E_a	Activation energy	—
β	C_{rate} stress coefficient	—

References

1. Liu, L.; He, G.; Wu, M.; Liu, G.; Zhang, H.; Chen, Y.; Shen, J.; Li, S. Climate change impacts on planned supply–demand match in global wind and solar energy systems. *Nat. Energy* **2023**, *8*, 870–880. [[CrossRef](#)]
2. Blaabjerg, F.; Ma, K. Future on power electronics for wind turbine systems. *IEEE J. Emerg. Sel. Top. Power Electron.* **2013**, *1*, 139–152. [[CrossRef](#)]
3. Zakeri, B.; Syri, S. Electrical energy storage systems: A comparative life cycle cost analysis. *Renew. Sustain. Energy Rev.* **2015**, *42*, 569–596. [[CrossRef](#)]
4. Dunn, B.; Kamath, H.; Tarascon, J.-M. Electrical energy storage for the grid: A battery of choices. *Science* **2011**, *334*, 928–935. [[CrossRef](#)] [[PubMed](#)]
5. Keil, P. Aging of lithium-ion batteries in electric vehicles. *World Electr. Veh. J.* **2015**, *7*, 41–51. [[CrossRef](#)]
6. Yang, X.-G.; Leng, Y.; Zhang, G.; Ge, S.; Wang, C.-Y. Modeling of lithium plating induced aging of lithium-ion batteries: Transition from linear to nonlinear aging. *J. Power Sources* **2017**, *360*, 28–40. [[CrossRef](#)]
7. Severson, K.A.; Attia, P.M.; Jin, N.; Perkins, N.; Jiang, B.; Yang, Z.; Chen, M.H.; Aykol, M.; Herring, P.K.; Fraggedakis, D. Data-driven prediction of battery cycle life before capacity degradation. *Nat. Energy* **2019**, *4*, 383–391. [[CrossRef](#)]
8. Li, T.; Zhou, Z.; Thelen, A.; Howey, D.A.; Hu, C. Predicting battery lifetime under varying usage conditions from early aging data. *Cell Rep. Phys. Sci.* **2024**, *5*, 101891. [[CrossRef](#)]
9. Sugiarto, L.; Huang, Z.; Lu, Y.-C. Battery Lifetime Prediction Using Surface Temperature Features from Early Cycle Data. *Energy Environ. Sci.* **2025**, *18*, 2511–2523. [[CrossRef](#)]
10. Celik, B.; Sandt, R.; dos Santos, L.C.P.; Spatschek, R. Prediction of battery cycle life using early-cycle data, machine learning and data management. *Batteries* **2022**, *8*, 266. [[CrossRef](#)]
11. Nájera, J.; Arribas, J.; De Castro, R.; Núñez, C. Semi-empirical ageing model for LFP and NMC Li-ion battery chemistries. *J. Energy Storage* **2023**, *72*, 108016. [[CrossRef](#)]
12. Kim, J.; Sin, S.; Kim, J. Early remaining-useful-life prediction applying discrete wavelet transform combined with improved semi-empirical model for high-fidelity in battery energy storage system. *Energy* **2024**, *297*, 131285. [[CrossRef](#)]
13. Marongiu, A.; Roscher, M.; Sauer, D.U. Influence of the vehicle-to-grid strategy on the aging behavior of lithium battery electric vehicles. *Appl. Energy* **2015**, *137*, 899–912. [[CrossRef](#)]
14. Serrao, L.; Chehab, Z.; Guezenne, Y.; Rizzoni, G. An aging model of Ni-MH batteries for hybrid electric vehicles. In Proceedings of the 2005 IEEE Vehicle Power and Propulsion Conference, Chicago, IL, USA, 7 September 2005; p. 8.
15. Ortega-Vazquez, M.A. Optimal scheduling of electric vehicle charging and vehicle-to-grid services at household level including battery degradation and price uncertainty. *IET Gener. Transm. Distrib.* **2014**, *8*, 1007–1016. [[CrossRef](#)]
16. Kavousi-Fard, A.; Niknam, T.; Fotuhi-Firuzabad, M. Stochastic reconfiguration and optimal coordination of V2G plug-in electric vehicles considering correlated wind power generation. *IEEE T Sustain. Energ.* **2015**, *6*, 822–830. [[CrossRef](#)]
17. Nunna, H.K.; Battula, S.; Doolla, S.; Srinivasan, D. Energy management in smart distribution systems with vehicle-to-grid integrated microgrids. *IEEE Trans. Smart Grid* **2016**, *9*, 4004–4016. [[CrossRef](#)]
18. Wan, Y.; Gebbran, D.; Subroto, R.K.; Dragičević, T. Optimal Day-ahead Scheduling of Fast EV Charging Station With Multi-stage Battery Degradation Model. *IEEE Trans. Energy Convers.* **2023**, *39*, 872–883. [[CrossRef](#)]
19. Motapon, S.N.; Lachance, E.; Dessaint, L.-A.; Al-Haddad, K. A generic cycle life model for lithium-ion batteries based on fatigue theory and equivalent cycle counting. *IEEE Open J. Ind. Electron. Soc.* **2020**, *1*, 207–217. [[CrossRef](#)]
20. Saldaña, G.; San Martín, J.I.; Zamora, I.; Asensio, F.J.; Onederra, O.; González, M. Empirical electrical and degradation model for electric vehicle batteries. *IEEE Access* **2020**, *8*, 155576–155589. [[CrossRef](#)]
21. Rechkemmer, S.K.; Zang, X.; Zhang, W.; Sawodny, O. Empirical Li-ion aging model derived from single particle model. *J. Energy Storage* **2019**, *21*, 773–786. [[CrossRef](#)]
22. Vilsen, S.B.; Stroe, D.-I. Battery state-of-health modelling by multiple linear regression. *J. Clean. Prod.* **2021**, *290*, 125700. [[CrossRef](#)]
23. Zhao, H.; Meng, J.; Peng, Q. Early perception of Lithium-ion battery degradation trajectory with graphical features and deep learning. *Appl. Energ.* **2025**, *381*, 125214. [[CrossRef](#)]

24. Patrizi, G.; Martiri, L.; Pievatolo, A.; Magrini, A.; Meccariello, G.; Cristaldi, L.; Nikiforova, N.D. A review of degradation models and remaining useful life prediction for testing design and predictive maintenance of Lithium-Ion Batteries. *Sensors* **2024**, *24*, 3382. [[CrossRef](#)] [[PubMed](#)]
25. Almutairi, Z.A.; Eltamaly, A.M.; El Khereiji, A.; Al Nassar, A.; Al Rished, A.; Al Saheel, N.; Al Marqabi, A.; Al Hamad, S.; Al Harbi, M.; Sherif, R. Modeling and Experimental Determination of Lithium-Ion Battery Degradation in Hot Environment. In Proceedings of the 2022 23rd International Middle East Power Systems Conference (MEPCON), Cairo, Egypt, 13–15 December 2022; pp. 1–8.
26. Ganterbein, S.; Schönleber, M.; Weiss, M.; Ivers-Tiffée, E. Capacity fade in lithium-ion batteries and cyclic aging over various state-of-charge ranges. *Sustainability* **2019**, *11*, 6697. [[CrossRef](#)]
27. Vetter, J.; Novák, P.; Wagner, M.R.; Veit, C.; Möller, K.-C.; Besenhard, J.; Winter, M.; Wohlfahrt-Mehrens, M.; Vogler, C.; Hammouche, A. Ageing mechanisms in lithium-ion batteries. *J. Power Sources* **2005**, *147*, 269–281. [[CrossRef](#)]
28. Safari, M.; Delacourt, C. Modeling of a commercial graphite/LiFePO₄ cell. *J. Electrochem. Soc.* **2011**, *158*, A562. [[CrossRef](#)]
29. Ruiz, P.L.; Damianakis, N.; Mouli, G.R.C. Physics-based and Data-driven Modeling of Degradation Mechanisms for Lithium-Ion Batteries—A Review. *IEEE Access* **2025**, *13*, 21164–21189. [[CrossRef](#)]
30. Liu, C.; Li, H.; Li, K.; Wu, Y.; Lv, B. Deep Learning for State of Health Estimation of Lithium-Ion Batteries in Electric Vehicles: A Systematic Review. *Energies* **2025**, *18*, 1463. [[CrossRef](#)]
31. Chen, J.; Han, X.; Sun, T.; Zheng, Y. Analysis and prediction of battery aging modes based on transfer learning. *Appl. Energ.* **2024**, *356*, 122330. [[CrossRef](#)]
32. Yarimca, G.; Cetkin, E. Review of cell level battery (calendar and cycling) aging models: Electric vehicles. *Batteries* **2024**, *10*, 374. [[CrossRef](#)]
33. Zhang, Y.; Peng, Z.; Guan, Y.; Wu, L. Prognostics of battery cycle life in the early-cycle stage based on hybrid model. *Energy* **2021**, *221*, 119901. [[CrossRef](#)]
34. Rahamanian, F.; Lee, R.M.; Linzner, D.; Michel, K.; Merker, L.; Berkes, B.B.; Nuss, L.; Stein, H.S. Attention towards chemistry agnostic and explainable battery lifetime prediction. *NPJ Comput. Mater.* **2024**, *10*, 100. [[CrossRef](#)]
35. Zhang, H.; Li, Y.; Zheng, S.; Lu, Z.; Gui, X.; Xu, W.; Bian, J. Battery lifetime prediction across diverse ageing conditions with inter-cell deep learning. *Nat. Mach. Intell.* **2025**, *7*, 270–277. [[CrossRef](#)]
36. Zhang, H.; Su, Y.; Altaf, F.; Wik, T.; Gros, S. Interpretable battery cycle life range prediction using early cell degradation data. *IEEE Trans. Transp. Electrif.* **2022**, *9*, 2669–2682. [[CrossRef](#)]
37. Haris, M.; Hasan, M.N.; Qin, S. Degradation curve prediction of lithium-ion batteries based on knee point detection algorithm and convolutional neural network. *IEEE Trans. Instrum. Meas.* **2022**, *71*, 1–10. [[CrossRef](#)]
38. Choi, Y.; Ryu, S.; Park, K.; Kim, H. Machine learning-based lithium-ion battery capacity estimation exploiting multi-channel charging profiles. *IEEE Access* **2019**, *7*, 75143–75152. [[CrossRef](#)]
39. Kohtz, S.; Xu, Y.; Zheng, Z.; Wang, P. Physics-informed machine learning model for battery state of health prognostics using partial charging segments. *Mech. Syst. Signal Process.* **2022**, *172*, 109002. [[CrossRef](#)]
40. Zhang, Y. *Data-Driven Battery Aging Diagnostics and Lifetime Extension*; Chalmers: Gothenburg, Sweden, 2024.
41. Chou, J.-H.; Wang, F.-K.; Lo, S.-C. A novel fine-tuning model based on transfer learning for future capacity prediction of lithium-ion batteries. *Batteries* **2023**, *9*, 325. [[CrossRef](#)]
42. Tang, W.; Chen, J.; Chen, D. Predicting EV battery state of health using long short term degradation feature extraction and FEA TimeMixer. *Sci. Rep.* **2025**, *15*, 2200. [[CrossRef](#)] [[PubMed](#)]
43. Barré, A.; Deguilhem, B.; Grolleau, S.; Gérard, M.; Suard, F.; Riu, D. A review on lithium-ion battery ageing mechanisms and estimations for automotive applications. *J. Power Sources* **2013**, *241*, 680–689. [[CrossRef](#)]
44. Gailani, A.; Al-Greer, M.; Short, M.; Crosbie, T. Degradation cost analysis of li-ion batteries in the capacity market with different degradation models. *Electronics* **2020**, *9*, 90. [[CrossRef](#)]
45. Singh, P.; Chen, C.; Tan, C.M.; Huang, S.-C. Semi-empirical capacity fading model for SoH estimation of Li-ion batteries. *Appl. Sci.* **2019**, *9*, 3012. [[CrossRef](#)]
46. Safari, M.; Delacourt, C. Aging of a commercial graphite/LiFePO₄ cell. *J. Electrochem. Soc.* **2011**, *158*, A1123. [[CrossRef](#)]
47. Schmalstieg, J.; Käbitz, S.; Ecker, M.; Sauer, D.U. A holistic aging model for Li (NiMnCo)O₂ based 18650 lithium-ion batteries. *J. Power Sources* **2014**, *257*, 325–334. [[CrossRef](#)]
48. Birk, C.R.; Roberts, M.R.; McTurk, E.; Bruce, P.G.; Howey, D.A. Degradation diagnostics for lithium ion cells. *J. Power Sources* **2017**, *341*, 373–386. [[CrossRef](#)]
49. Almutairi, Z.; Alzahrani, A.; Eltamaly, A.M. Optimal Design of Zero-Carbon Smart Grid for NEOM City. In Proceedings of the 2024 25th International Middle East Power System Conference (MEPCON), Cairo, Egypt, 17–19 December 2024; pp. 1–8.
50. Dubarry, M.; Vuillaume, N.; Liaw, B.Y. Origins and accommodation of cell variations in Li-ion battery pack modeling. *Int. J. Energy Res.* **2010**, *34*, 216–231. [[CrossRef](#)]

51. Omenya, F.; Paiss, M.; Li, X.; Reed, D. Energy and power evolution over the lifetime of a battery. *ACS Energy Lett.* **2023**, *8*, 2707–2710. [[CrossRef](#)]
52. Dufo-López, R.; Cortés-Arcos, T.; Artal-Sevil, J.S.; Bernal-Agustín, J.L. Comparison of lead-acid and li-ion batteries lifetime prediction models in stand-alone photovoltaic systems. *Appl. Sci.* **2021**, *11*, 1099. [[CrossRef](#)]
53. Huang, J.; Wang, S.; Xu, W.; Fernandez, C.; Fan, Y.; Chen, X. An improved rainflow algorithm combined with linear criterion for the accurate Li-ion battery residual life prediction. *Int. J. Electrochem. Sci.* **2021**, *16*, 21075. [[CrossRef](#)]
54. Tran, D.; Khambadkone, A.M. Energy management for lifetime extension of energy storage system in micro-grid applications. *IEEE Trans. Smart Grid* **2013**, *4*, 1289–1296. [[CrossRef](#)]
55. Byrd, R.H.; Lu, P.; Nocedal, J.; Zhu, C. A limited memory algorithm for bound constrained optimization. *SIAM J. Sci. Comput.* **1995**, *16*, 1190–1208. [[CrossRef](#)]
56. Eltamaly, A.M. Musical chairs algorithm for parameters estimation of PV cells. *Sol. Energy* **2022**, *241*, 601–620. [[CrossRef](#)]
57. Eltamaly, A.M.; Rabie, A.H. A Novel Musical Chairs Optimization Algorithm. *Arab. J. Sci. Eng.* **2023**, *48*, 10371–10403. [[CrossRef](#)]
58. Eltamaly, A.M. A novel musical chairs algorithm applied for MPPT of PV systems. *Renew. Sust. Energ. Rev.* **2021**, *146*, 111135. [[CrossRef](#)]
59. Almutairi, Z.A.; Eltamaly, A.M. Synergistic Effects of Energy Storage Systems and Demand-Side Management in Optimizing Zero-Carbon Smart Grid Systems. *Energies* **2024**, *17*, 5637. [[CrossRef](#)]
60. Eltamaly, A.M. Smart Decentralized Electric Vehicle Aggregators for Optimal Dispatch Technologies. *Energies* **2023**, *16*, 8112. [[CrossRef](#)]
61. Almutairi, Z.; Bheyan, H.A.; Al-Ansary, H.; Eltamaly, A.M. Reducing Lithium-Ion Battery Testing Costs Through Strategic Sample Optimization. *Processes* **2025**, *13*, 2030. [[CrossRef](#)]
62. Eltamaly, A.M. A novel energy storage and demand side management for entire green smart grid system for NEOM city in Saudi Arabia. *Energy Storage* **2023**, *6*, e515. [[CrossRef](#)]
63. Eltamaly, A.M. Optimal control parameters for bat algorithm in maximum power point tracker of photovoltaic energy systems. *Int. T Electr. Energy* **2021**, *31*, e12839. [[CrossRef](#)]
64. Mirjalili, S. SCA: A sine cosine algorithm for solving optimization problems. *Knowl. Based Syst.* **2016**, *96*, 120–133. [[CrossRef](#)]
65. Eltamaly, A.M. A Novel Strategy for Optimal PSO Control Parameters Determination for PV Energy Systems. *Sustainability* **2021**, *13*, 1008. [[CrossRef](#)]

Disclaimer/Publisher’s Note: The statements, opinions and data contained in all publications are solely those of the individual author(s) and contributor(s) and not of MDPI and/or the editor(s). MDPI and/or the editor(s) disclaim responsibility for any injury to people or property resulting from any ideas, methods, instructions or products referred to in the content.